Monthly Notices of the ROYAL ASTRONOMICAL SOCIETY

MNRAS **521,** 5418–5439 (2023) https://doi.org/10.1093/mnras/stad830
Advance Access publication 2023 March 20

Optical polarization and spectral properties of the hydrogen-poor superluminous supernovae SN 2021bnw and SN 2021fpl

F. Poidevin [1,2]★ C. M. B. Omand,[3]★ Réka Könyves-Tóth,[4,5,6]★ I. Pérez-Fournon,[1,2] R. Clavero,[1,2] S. Geier,[1,2,7] C. Jimenez Angel,[1,2] R. Marques-Chaves[8] and R. Shirley[9,10]

[1]*Instituto de Astrofisíca de Canarias, E-38200 La Laguna, Tenerife, Canary Islands, Spain*
[2]*Departamento de Astrofísica, Universidad de La Laguna (ULL), E-38206 La Laguna, Tenerife, Spain*
[3]*The Oskar Klein Centre, Department of Astronomy, Stockholm University, AlbaNova, E-10691 Stockholm, Sweden*
[4]*Konkoly Observatory, CSFK, Konkoly-Thege M. út 15-17, Budapest, 1121, Hungary*
[5]*Department of Experimental Physics, Institute of Physics, University of Szeged, Dóm tér 9, Szeged, 6720, Hungary*
[6]*ELTE Eötvös Loránd University, Gothard Astrophysical Observatory, 9700 Szombathely, Szent Imre h. u. 112, Hungary*
[7]*GRANTECAN, Cuesta de San José s/n, E-38712 Breña Baja, La Palma, Spain*
[8]*Geneva Observatory, University of Geneva, Chemin Pegasi 51, CH-1290 Versoix, Switzerland*
[9]*Astronomy Centre, Department of Physics & Astronomy, University of Southampton, Southampton SO17 1BJ, UK*
[10]*Institute of Astronomy, University of Cambridge, Madingley Road, Cambridge CB3 0HA, UK*

Accepted 2023 March 9. Received 2023 March 3; in original form 2022 October 31

ABSTRACT

New optical photometric, spectroscopic, and imaging polarimetry data are combined with publicly available data to study some of the physical properties of the two hydrogen-poor superluminous supernovae (SLSNe) SN 2021bnw and SN 2021fpl. For each SLSN, the best-fitting parameters obtained from the magnetar model with Modular Open-Source Fitter for Transients do not depart from the range of parameter obtained on other SLSNe discussed in the literature. A spectral analysis with SYN++ shows that SN 2021bnw is a W type, fast evolver, while SN 2021fpl is a 15bn type, slow evolver. The analysis of the polarimetry data obtained on SN 2021fpl at four epochs (+1.8, +20.6, +34.1, and +43.0 d, rest frame) shows $>3\sigma$ polarization detections in the range of 0.8–1 per cent. A comparison of the spectroscopy data suggests that SN 2021fpl underwent a spectral transition a bit earlier than SN 2015bn, during which, similarly, it could have underwent a polarization transition. The analysis of the polarimetry data obtained on SN 2021bnw does not show any departure from symmetry of the photosphere at an empirical diffusion time-scale of $\approx$2 (+81.1 d rest frame). This result is consistent with those on the sample of W-type SLSN observed at empirical diffusion time-scale ≤ 1 with that technique, even though it is not clear the effect of limited spectral windows varying from one object to the other. Measurements at higher empirical diffusion time-scale may be needed to see any departure from symmetry as it is discussed in the literature for SN 2017egm.

Key words: techniques: photometric – techniques: polarimetric – techniques: spectroscopic – *(stars:)* supernovae: general – *(stars:)* supernovae: individual: LSQ14mo, SN 2015bn, SN 2017egm, SN 2018bsz, SN 2020ank, SN 2020znr, SN 2021bnw, SN 2021fpl.

1 INTRODUCTION

Hydrogen-poor (H-poor) superluminous supernovae (SLSNe) have been discovered about 15-yr ago (see reviews by Howell 2017; Moriya, Sorokina & Chevalier 2018; Gal-Yam 2019; Chen 2021). While the spectral classification frequency of such transients is quite low ($\approx$1 per cent) with respect to other types of supernovae (SNe; e.g. Nicholl 2021), spectroscopic and photometric follow-ups of H-poor SLSNe (SLSN-I) by several surveys like, among others, the Palomar Transient Factory (PTF; Rau et al. 2009) and its intermediate version (intermediate PTF), the Dark Energy Survey (Angus et al. 2019), and more recently the Zwicky Transient Facility (ZTF; Bellm et al. 2019), provide a large amount of data allowing more and more discoveries and time-evolution studies of individual objects (e.g. Könyves-Tóth et al. 2020; Kumar et al. 2020), as well as statistical analysis of relatively large samples (e.g. Quimby et al. 2018; Angus et al. 2019; Könyves-Tóth & Vinkó 2021; Chen et al. 2023a, b). From the light curves and spectra analyses, several models have been proposed to explain the mechanisms behind the radiate total energies of $\approx 10^{51}$ erg from such objects. The current best models are those of a central engine consisting of fall-back accretion on a compact object (Dexter & Kasen 2013), or the spin-down of a newly formed magnetar (Kasen & Bildsten 2010; Woosley 2010). More recently, Könyves-Tóth & Vinkó (2021) found that H-poor SLSNe can be divided in two distinct groups according to their pre-maximum spectra. The members of the first group show the W-shaped absorption feature well discussed in the literature, and identified as due to O II. This feature is not observed in the second group, whose spectral shape is more similar to that of SN 2015bn. Each of these groups can also be classified as fast or slow evolvers

★ E-mail: fpoidevin@iac.es (FP); conor.omand@astro.su.se (CMBO); konyvestoth.reka@csfk.org (RKT)

Table 1. Information about SN 2021bnw and SN 2021fpl. Photometry and coordinates of the host candidate of SN 2021bnw are from the Dark Energy Camera Legacy Survey (DECaLS). Upper magnitude limits at the position of SN 2021fpl are from Panoramic Survey Telescope and Rapid Response System (Pan-STARRS1).

Object Name	RA_{SN} (°)	Dec_{SN} (°)	redshift	μ (mag)	Host candidate	RA_{HOST} (°)	Dec_{HOST} (°)	g (mag)	r (mag)	z (mag)
2021bnw	163.467 375	+ 12.558 05	0.098	−38.24	Brick: 1635p125, Objid: 1948	163.4678	12.5581	19.79	19.31	19.01
2021fpl	303.577 583	− 18.182 381	0.115	−38.59	Orphan SLSN-I?	RA_{SN}	Dec_{SN}	>23.6	>23.0	>22.6

based on the photospheric velocities around maximum, even though this classification may be limited by the size of the sample and the lack of object having intermediate photospheric velocities.

Polarimetry follow-ups of SLSN-I, on the other hand, are quite scarce. So far, no more than 10 sources have been observed with linear polarimetry (Leloudas et al. 2015, 2017a; Brown et al. 2016; Inserra et al. 2016; Cikota et al. 2018; Lee 2019, 2020; Maund et al. 2019, 2020, 2021; Saito et al. 2020; Poidevin et al. 2022; Pursiainen et al. 2022), among which three have also been observed with spectropolarimetry (2015bn, 2017egm, and 2018bsz by Inserra et al. 2016, Saito et al. 2020, and Pursiainen et al. 2022, respectively), and two have been probed with circular polarimetry (OGLE16dmu and LSQ14mo by Cikota et al. 2018). The main difficulty encountered by such surveys comes from the Galactic contribution and possible contributions from the SLSNe hosts possibly combined with light dilution effects by the hosts (see Leloudas et al. 2022). Such problems can in principle be tackled with spectropolarimetry if specific spectral windows in the spectra can be used to isolate the host galaxy contribution to get intrinsic polarization estimates of the SLSN (see Saito et al. 2020). Alternatively, if the host galaxy is bright enough, one could measure its intrinsic level of polarization months or years after the SLSN has faded away. This would give an integrated estimate of the level of polarization of the Galaxy that could be compared afterward with the polarimetry measurements of the SLSN. If such measurements are not possible or reach observation limit sensitivities, one could still rely on the low level of polarization measured on many systems before maximum light. Most of the current available measurements obtained so far with linear polarimetry show that once the Galactic interstellar polarization (ISP) contributions have been taken into account, one can expect low degrees of polarization of order fractions of a per cent before maximum light. Such results suggest that the host contribution is very low and that the light of the SLSN pervading the host ISM is not significantly polarized by magnetically aligned dust grains (see e.g. discussion in Poidevin et al. 2022). From that point, any increase in the degree of polarization measured at later phases could be attributed to a loss of the symmetry of the photosphere. Such measurements have been obtained on SN 2015bn with linear polarimetry (Leloudas et al. 2017a) and were found consistent with the results obtained with spectropolarimetry (Inserra et al. 2016). The increase of polarization is observed along a uniform polarization angle direction which is interpreted as the axis of symmetry of the inner photosphere. Alternatively, a change of polarization could come from the interaction of the photosphere with a possible disc-like, clumpy circumstellar medium (CSM) with emitting regions. This has been observed on SN 2018bsz and discussed by Pursiainen et al. (2022).

In this work, we present the results obtained on the second and third target from a 10-h linear polarimetry survey conducted mainly during 2021, and designed to explore the frequency of objects like SN 2015bn and SN 2017egm. Along this work, we use the *Planck* 2018 flat Lambda cold dark matter cosmology model ($\Omega_0 = 0.31$, $H_0 = 67.7$ km s^{-1}; Planck Collaboration I 2020).

2 H-POOR SLSN SAMPLE AND HOSTS ASSOCIATIONS

Basic information about the two SLSN-I, SN 2021bnw and SN 2021fpl, and their possible hosts is given in Table 1.

2.1 SN 2021bnw

SN 2021bnw [ZTF object ZTF21aagpymw, Pan-STARRS1 object PS21ajy, Asteroid Terrestrial-impact Last Alert System (ATLAS) object ATLAS21dpf, and *Gaia* object Gaia21caf] was discovered by Fremling (2021) on 2021 February 3 from ZTF[1] public alerts (Bellm et al. 2019). The discovery magnitude obtained with the ZTF-cam mounted on the Palomar 1.2 m *Oschin* was of 21.07 mag in the g-filter (AB system). The transient was classified the following day as a SLSN-I at a redshift (z) = 0.098 by Magee et al. (2021) (see also Terwel et al. 2021) from the analysis of a spectrum obtained by the extended Public ESO Spectroscopic Survey of Transient Objects (Smartt et al. 2017) collaboration. The spectrum is publicly available on the Transient Name Server[2] (TNS).

SN 2021bnw is very likely associated with the galaxy observed in the DECaLS[3], Data Release 9 (DR9) at position (RA, Dec) = (163.4678°, +12.5581°, J2000), of apparent magnitudes $g = 19.79$, $r = 19.31$, and $z = 19.01$ mag, i.e. of absolute magnitudes −18.45, −18.93, and −19.23 mag, respectively, assuming it is at the same redshift as the SLSN at $z = 0.098$. This galaxy has also been observed in the Sloan Digitized Sky Survey (SDSS) imaging DR9 as is identified as SDSS J105352.17+123328.5 but the photometry obtained on that source may be unreliable.[4]

2.2 SN 2021fpl

SN 2021fpl (ZTF object ZTF21aaxwpyv, Pan-STARRS1 object PS21evf, ATLAS object ATLAS21iao, and *Gaia* object Gaia21ckf) was discovered by Tonry et al. (2021) on 2021 March 16 from the ATLAS survey. The discovery magnitude was of 18.192 mag in the ATLAS Orange-filter (AB system). The transient was classified on 2021 April 26 as an SLSN-I at a redshift (z) = 0.115 by Deckers et al. (2021a) (see also Deckers et al. 2021b) from the analysis of a spectrum obtained with the *Liverpool Telescope* (*LT*) SPectrograph for the Rapid Acquisition of Transients (SPRAT) (Steele et al. 2004; Piascik et al. 2014). This spectrum is publicly available on the TNS.[5]

The field of view of SN 2021fpl was observed by the Pan-STARRS1 (Chambers et al. 2016) making this SLSN looking as an orphan SN, or with no clear association. Magnitude upper limits

[1]Zwicky Transient Facility, https://www.ztf.caltech.edu.
[2]Transient Name Server, https://www.wis-tns.org/2021bnw.
[3]Legacy Survey, https://www.legacysurvey.org/.
[4]http://skyserver.sdss.org/dr17/VisualTools/explore/summary
[5]Transient Name Server, https://www.wis-tns.org/2021fpl.

from PanSTARSS-1 forced photometry are displayed in Table 1 for indication. Footprints from the DECaLS DR9 and SDSS DR17 surveys do not cover the field of view of SN 2021fpl.

3 DATA

3.1 Photometry

The compilation of the photometry of SN 2021bnw and SN 2021fpl used in this work is listed in Tables D1, D2, and D3, and in Tables D4, D5, D6, and D7, respectively (see online supplementary material).

3.1.1 ZTF

The ZTF *g*- and *r*-band public photometry data obtained on SN 2021bnw (ZTF21aagpymw), and on SN 2021fpl (ZTF21aaxwpyv) were all retrieved from the Lasair broker[6] (Smith et al. 2019).

3.1.2 LT IO:O

Additional photometry observations were taken on SN 2021fpl in *u*, *g*, *r*, *i*, and *z* bands with the *LT* IO:O instrument. The data were reduced using the AUTOmated PHotometry Of Transients (`AutoPhOT`)[7] package (Brennan & Fraser 2022). The main steps of the `AutoPhOT` pipeline are as follows. The pipeline builds a model of the point spread function (PSF) in an image from bright isolated sources in the field, or uses aperture photometry if no suitable sources are present. The instrumental magnitude is then measured from a fit of the PSF to the transient. The instrumental magnitude is calibrated on to the standard system (AB magnitudes for Sloan-like filters) from an estimate of the zero-point in each image which is obtained from comparisons with catalogued standards in the field. For *ugriz* filters, the zero-point was calculated from magnitudes of sources in the field observed by the SkyMapper Southern Observatory (Onken et al. 2019). A signal-to-noise ratio (SNR) of 5 was used to filter out bad photometry estimates. The log of the observations is displayed in Table A1.

3.1.3 ATLAS

The ATLAS forced photometry data were retrieved from the ATLAS public server[8] (Tonry et al. 2018). The data were clipped and binned using the publicly available code plot_atlas_fp.py.[9] ATLAS data of SN 2021bnw were grouped in bins of 1 d. ATLAS data of SN 2021fpl were showing a bit more dispersion than those of 2021bnw and for that reason were binned in bins of 2 d.

3.1.4 Light curves

The absolute magnitude light curves of SN 2021bnw and of SN 2021fpl are displayed in Fig. 1, top and bottom plots, respectively. For each source, the distance modulus, $\mu = m - M$, displayed in Table 1 was used to convert the apparent magnitude (see tables in Appendix D) to absolute magnitude. Both SLSNe peak at absolute magnitudes close to −21 mag. The public ZTF data and the public

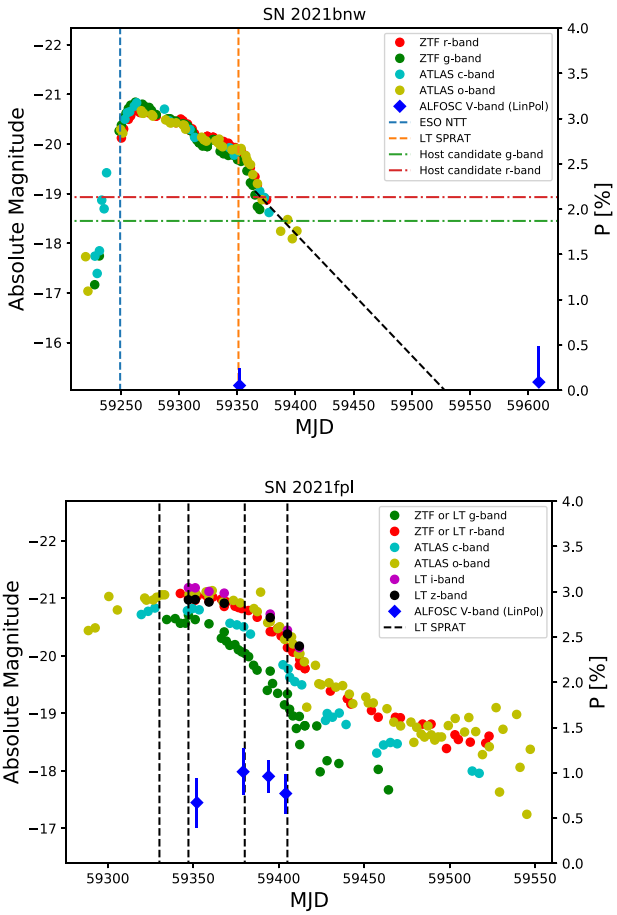

Figure 1. Top plot: ZTF *g*- and *r*-band, and ATLAS *c*- and *o*-band absolute light curve of SN 2021bnw. The epochs when spectroscopy was obtained are shown with dashed lines. The absolute magnitudes of the host candidate are shown with the horizontal dashed lines. A linear fit to the last eight points of the light curve is shown with the dark dashed line. The linear polarization degree, *P*, is also shown by the diamond symbol. The scale is given on the right-axis. Bottom plot: Same as top plot for SN 2021fpl with additional photometry obtained from the *LT* in *g*, *r*, *i*, and *z* bands (see Section 3.1.2 and Table A1 in the online supplementary material).

stacked and binned ATLAS data available for each of these sources are displayed in both plots. The additional photometry obtained on SN 2021fpl with the *LT* IO:O is displayed on the bottom plot in Fig. 1. Spectroscopy was obtained at several epochs on each source and will be discussed in Section 3.2. The epochs of spectroscopy are marked with the vertical dashed lines in each plots. Polarimetry, was also obtained at several epochs, as will be discussed in Section 3.3. The fractions of polarization are shown by blue diamonds symbols (the polarization scales are given in the right-axis of each plot).

3.2 Spectroscopy

A summary of the spectroscopy obtained on SN 2021bnw and SN 2021fpl is given in Table B1 in the online supplementary material.

3.2.1 SN 2021bnw

Two spectra are available on this source. We retrieved the publicly available spectrum obtained at early phase (Fig. 1, top plot) from

[6] https://lasair.roe.ac.uk/object/
[7] https://github.com/Astro-Sean/autophot
[8] https://fallingstar-data.com/forcedphot/
[9] https://gist.github.com/thespacedoctor/86777fa5a9567b7939e8d84fd8cf6a76

TNS.[10] A second spectrum was obtained with the *LT* SPRAT. This spectrum was obtained about 1-d before polarimetry was obtained on SN 2021bnw. The two spectra obtained on SN 2021bnw are shown in Fig. 2, top plot. Also shown in the figure is the transmission of the *V* filter mounted on the Alhambra Faint Object Spectrograph and Camera (ALFOSC)[11] used to get linear polarimetry data discussed in the next section. The dashed line shows the imprint of the filter in the rest frame of the SN. We tested the classification and redshift of the two spectra of SN 2021bnw from a fitting template analysis with the SuperNova IDentification (SNID)[12] code (Blondin & Tonry 2007). To do so, we used the Quimby et al. (2018) spectra data base ingested in our custom SNID template library. The best match solutions displayed in Fig. 2, top plot, are consistent with the classification reported on TNS.[13]

3.2.2 SN 2021fpl

Four spectra are available on that source. The first publicly available *LT* SPRAT spectrum used by Deckers et al. (2021a) to classify SN 2021fpl was downloaded from TNS.[14] We obtained three more spectra on that source with *LT* SPRAT. All the spectra are displayed Fig. 2 (bottom plot).

3.3 Polarimetry

Polarimetry on SN 2021bnw and SN 2021fpl was obtained with ALFOSC on the *Nordic Optical Telescope* (*NOT*). The observation logs of the imaging polarimetry are displayed in Table C1 (see online supplementary material). Linear polarimetry is made using a half-wave plate in the Filter And POLarimetry (FAPOL) unit and a calcite plate mounted in the aperture wheel. The calcite plate provides the simultaneous measurement of the ordinary and the extraordinary components of two orthogonal polarized beams (see Fig. 3, top and bottom plots). The half-wave plate can be rotated in steps of 22.5° from 0° to 337.5°. As a standard, four angles are used (0°, 22.5°, 45°, and 67.5°), which we used during our observations as referred to with the factor 4 used in the exposure time calculations displayed in Table C1 (see online supplementary material). The data reduction of the polarimetry data was done using the same method and pipeline discussed in Poidevin et al. (2022). The photometry of the ordinary and extraordinary beams was done using aperture photometry. When taking multiple sequences of four half wave plate (HWP) angles (e.g. SN 2021flp was observed 6∗4∗90 s), the polarization was calculated by summing-up the fluxes from the ordinary and extraordinary beams to minimize uncertainty propagation. Indeed, if the polarization was calculated individually for each sequence and the Stokes parameters summed-up at the end of the process, one would have to propagate the uncertainties on Q and U and combine them all together. All the results and their interpretation will be discussed in Section 4.3.

3.3.1 SN 2021bnw

Polarimetry was obtained on SN 2021bnw at one phase, about +89-d after maximum light. A measurement was obtained almost 1-yr after maximum light (+347 d), when the SN was expected to be at least 3

[10]Transient Name Server, https://www.wis-tns.org/2021bnw.
[11]ALFOSC, http://www.not.iac.es/instruments/alfosc/
[12]https://people.lam.fr/blondin.stephane/software/snid/
[13]Transient Name Server, https://www.wis-tns.org/2021bnw.
[14]Transient Name Server, https://www.wis-tns.org/2021fpl.

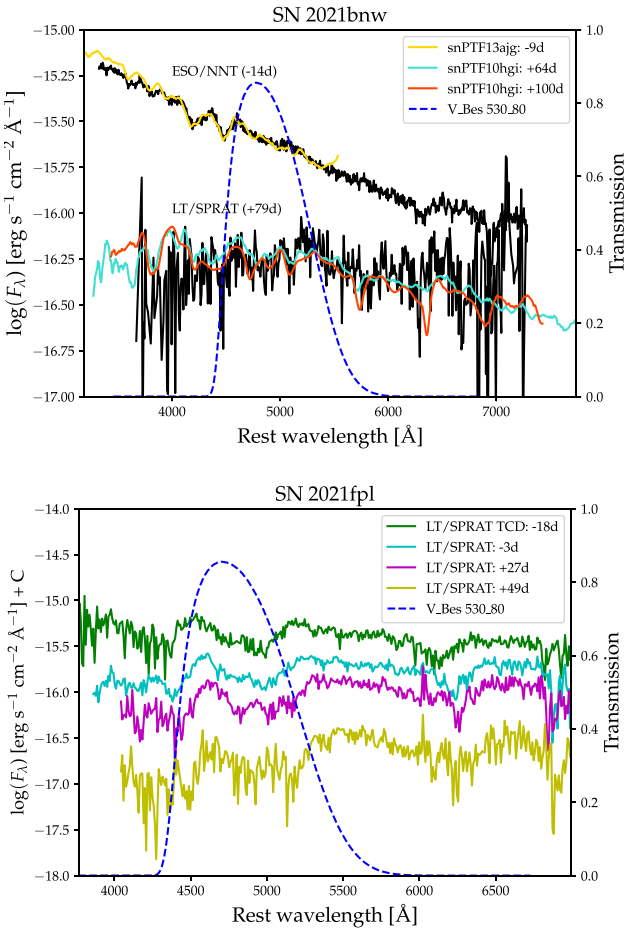

Figure 2. Spectra obtained on SN2021bnw (top plot) and SN2021fpl (bottom plot). The transmission curves of the V-band filter mounted on the ALFOSC are shown with the blue dashed lines in the wavelength range over which polarimetry is obtained in the rest frame of each SN.

to 4 magnitudes fainter than its host galaxy. This is suggested by the linear fit on the last point of the light curve of SN 2021bnw shown in Fig. 1 (top plot). The measurement at +347 d relative to peak brightness is therefore expected to reflect the polarization properties of the galaxy without any contribution from the SNe.

3.3.2 SN 2021fpl

Polarimetry of SN 2021fpl was obtained during four phases. A first measurement was obtained at an epoch close to maximum light (+2 d) and three additional measurements were obtained during the decreasing phase (+23, +38, and +48 d), before the radioactive decaying or shock-heated diffusion phase.

4 ANALYSIS

4.1 Light-curves modelling

There are several mechanisms which can be used to power an SLSNe light curve: nickel decay, CSM interaction, and a central magnetar. The large amount of nickel needed for SLSN light curves can only be produced in a pair instability SN, which requires an extremely massive progenitor and usually results of rise times of over 100 d (Kasen, Woosley & Heger 2011), which neither

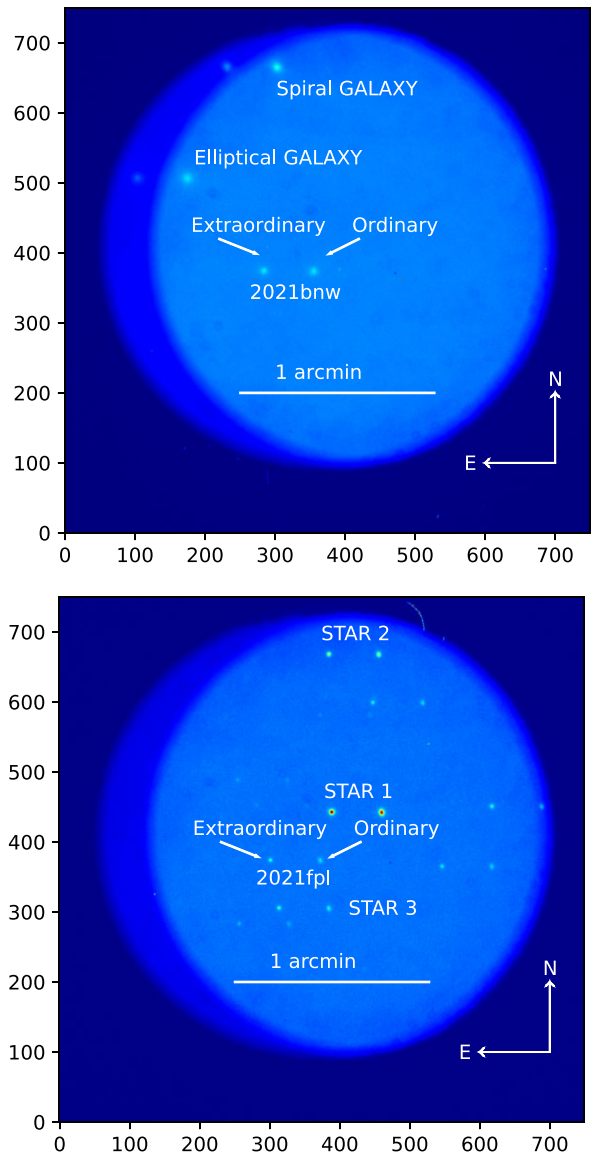

Figure 3. Top panel: Linear polarimetry of SN 2021bnw with ALFOSC in one of the *V*-band flat-field and bias-corrected data frame (file ALEe170044.fits) obtained with the half-wave plate at a position angle of 0.0°. Each pixel embeds the number of counts obtained after an exposure of 450 s. Imaging polarimetry was acquired through half-wave plates positions angles at 0.0°, 22.5°, 45.0° and 67.5°. The calcite plate splits the light from the several objects into ordinary images and extraordinary images separated by about 15 arcsec from each other. Bottom panel: Same as top panel for SN 2021fpl on one of the bias-corrected data frame (file ALEf280162.fits) obtained after an exposure time of 90 s.

SN 2021bnw nor SN 2021fpl show; pair instability SNe are also not expected to show significant polarization due to their quasi-spherical nature. Models using CSM interaction sometimes require unphysically high explosion energies to match both the kinetic and radiated energies inferred from observations (e.g. Kangas et al. 2022; Chen et al. 2023b) and analytic models tend to produce different results than numerical models (Moriya et al. 2018), leading to some inconsistencies in the interpretation of observations. As such, we only present light-curve fits using the magnetar model.

The multiband light curve of each SN is fitted using the 'slsn' magnetar spin-down model (Nicholl, Guillochon & Berger 2017c) in the Modular Open-Source Fitter for Transients (`MOSFiT`) code, which uses a Markov chain Monte Carlo algorithm to perform Bayesian parameter estimation for SN light curves (Guillochon et al. 2018). The Dynesty sampler (Higson et al. 2019; Speagle 2020), which utilizes dynamic nested sampling is used in the process. The uncertainty presented is only the statistical uncertainty in the fits, and does not include systematic uncertainty inherent in the simplified one-zone `MOSFiT` model.

The magnetar-model fits of SN 2021bnw and SN 2021fpl light curves are shown in Figs 4 and 5, respectively. The most physically relevant parameters are listed in Table 2, with their posteriors shown in Fig. 6 for SN 2021bnw, and in Fig. 7 for SN 2021fpl. The fits for both SNe are quite good, although there are some small undulations followed by a large decrease in the luminosity of SN 2021bnw at around 100-d post-peak that is not captured by the model. The physical parameters we find for SN 2021bnw (SN 2021fpl) are $B_\perp \approx 4 \times 10^{13}$ (8×10^{13}) G, $M_{\rm NS} \approx 1.6$ (1.7) $M_\odot$, $P_{\rm spin} \approx 4.6$ (1.4) ms, $\log(\kappa_\gamma) \approx -1.2$ (0.9) cm^2 g^{-1}, $M_{\rm ej} \approx 3.6$ (22) $M_\odot$, $T_{\rm min} \approx 9800$ (5500) K, and $v_{\rm ej} \approx 7900$ (6900) km s^{-1}; where $B_\perp$ is the magnetar magnetic field strength, $M_{\rm NS}$ is the neutron star mass, $P_{\rm spin}$ is the magnetar spin period, κ_γ is the gamma-ray opacity of the ejecta (Wang et al. 2015), $M_{\rm ej}$ is the ejecta mass, $T_{\rm min}$ is the photospheric plateau temperature, and $v_{\rm ej}$ is the ejecta velocity. These best-fitting parameters and uncertainties are the median and 1σ values from the one-dimensional (1D) posterior for each of the parameters. Although the parameters for these SNe are quite different, they are both representative of the extremes of the SLSN population (Nicholl et al. 2017c), with one extreme having high spin periods and low ejecta masses (like SN 2021bnw), and the other having low spin periods and high ejecta masses (like SN 2021fpl). The total kinetic energy of the ejecta for SN 2021bnw (SN 2021fpl) is calculated to be $E_{\rm K} \approx 1.3 \times 10^{51}$ (6.2×10^{51}) erg. The mass of the progenitor stars, $M_* = M_{\rm NS} + M_{\rm ej} \approx 5$ (23) $M_\odot$, which are consistent with the 3.6–40 $M_\odot$ range inferred in the mass distribution found by Blanchard et al. (2020).

We also find correlations between $B_\perp$, $M_{\rm NS}$, and $P_{\rm spin}$ in the 2D posterior distributions of these parameters, as in Poidevin et al. (2022), although the $P_{\rm spin}$ correlation in SN 2021fpl is not as strong as in SN 2020znr or SN 2021bnw. The cause of these correlations is still unknown.

The gamma-ray opacity is important when modelling a late-time decline in luminosity due to gamma-ray leakage. The leakage timescale is (Wang et al. 2015)

$$t_{\rm leak} \approx 80\ {\rm d} \left(\frac{\kappa_\gamma}{0.1\ {\rm cm^2\ g^{-1}}}\right)^{1/2} \left(\frac{M_{\rm ej}}{M_\odot}\right)^{1/2} \left(\frac{v_{\rm ej}}{10^4\ {\rm km\ s^{-1}}}\right)^{-1}. \quad (1)$$

For SN 2021bnw, $t_{\rm leak} \sim 150$ d, which is about when the light curve starts to decline. We also calculate the time when the optical depth of the ejecta $\tau_{\rm ej} = 1$, at (Nicholl et al. 2017c)

$$t_{\rm neb} = \left(3\kappa M_{\rm ej}/4\pi v_{\rm ej}^2\right)^{1/2}, \quad (2)$$

where κ is the opacity of the ejecta ($\kappa \approx 0.15$ cm^2 g^{-1} for both SNe). For SN 2021bnw, $t_{\rm neb} \sim 240$ d, which is much later than its light-curve decline. Even though the leakage time is correctly estimated, the model still cannot reproduce the observed luminosity decrease. This is likely due to a more complicated physical process than what is described by the model (Vurm & Metzger 2021), such as CSM interaction, dust formation (Omand, Kashiyama & Murase 2019), or

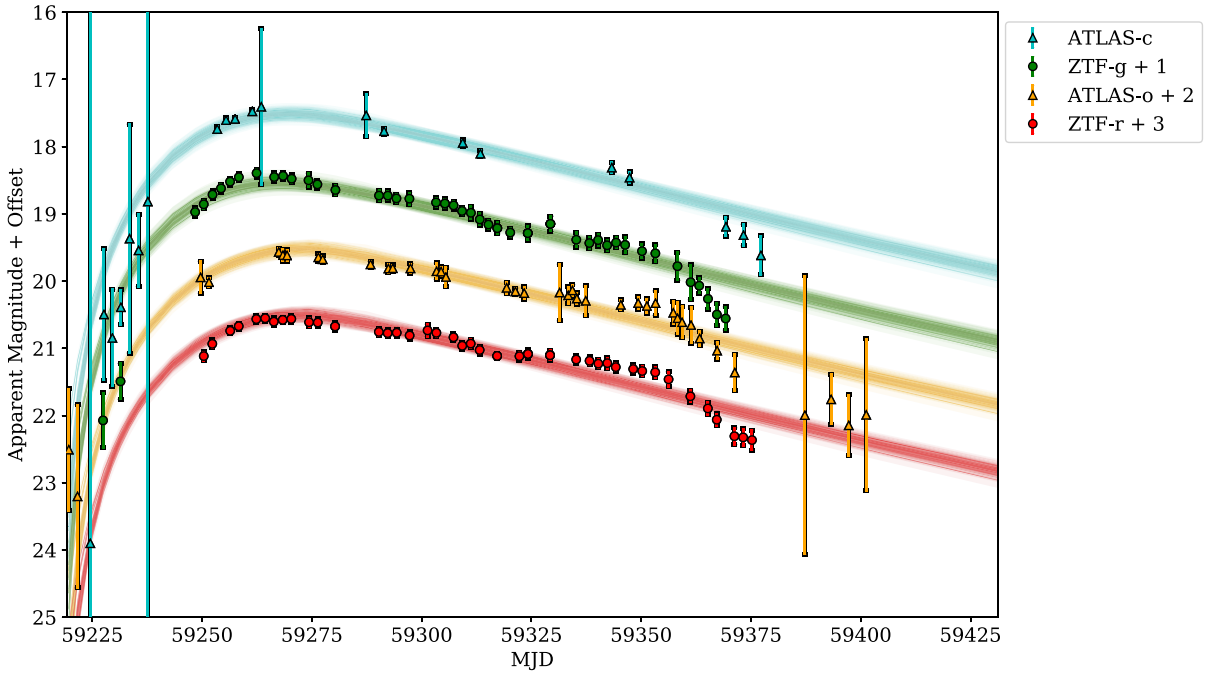

Figure 4. Multiband light curve of SN 2021bnw inferred from the magnetar model, with each band offset for clarity. The filled area shows the range of most likely models generated by `MOSFiT`. See Section 4.1 for details.

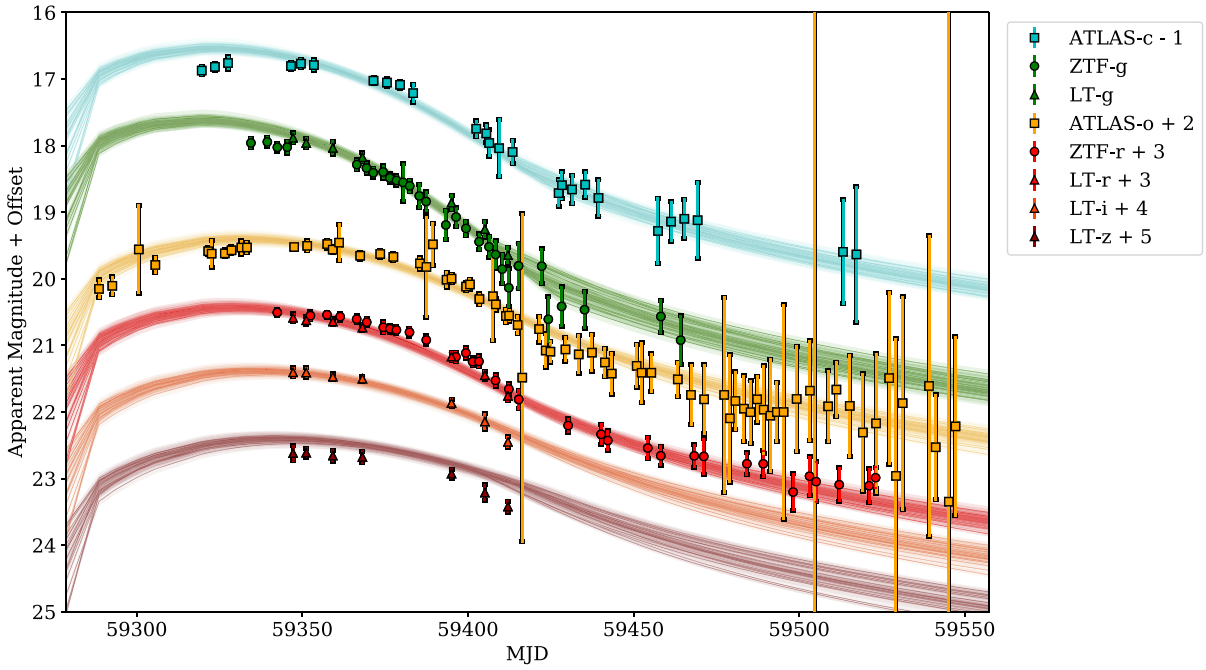

Figure 5. Multiband light curve of SN 2021fpl inferred from the magnetar model, with each band offset for clarity. The filled area shows the range of most likely models generated by `MOSFiT`. See Section 4.1 for details.

molecular cooling (Liljegren et al. 2022). The value of κ_γ is not well constrained for SN 2021fpl, since there is no observed luminosity decrease that looks consistent with gamma-ray leakage.

The ejecta velocities estimated by `MOSFiT` are not the same as the photospheric velocity, which can be estimated from spectra, since the photospheric velocity should decrease as the photosphere recedes further into the ejecta, while the ejecta velocity should remain relatively constant post-peak, with small increases and decreases due to acceleration from the pulsar wind nebula and collision with circumstellar material (CSM). However, the photospheric velocity at the light-curve maximum can be used as a proxy for the ejecta velocity (Könyves-Tóth & Vinkó 2021). The `MOSFiT` magnetar

Table 2. Median and 1σ best-fitting parameters for magnetar models obtained on SN 2021bnw and SN 2021fpl as discussed in Section 4.1.

Parameter symbol	Definition	Prior	Best-fitting value SN 2021bnw	Best-fitting value SN 2021fpl	Units
$B_{\perp}$	Magnetar magnetic field strength	[0.1,10]	$0.40^{+0.12}_{-0.11}$	$0.78^{+0.14}_{-0.17}$	10^{14} G
$M_{\rm NS}$	Neutron star mass	[1.0,2.0]	$1.58^{+0.26}_{-0.28}$	$1.71^{+0.19}_{-0.26}$	$M_{\odot}$
$P_{\rm spin}$	Magnetar spin period	[1,10]	$4.56^{+0.59}_{-0.64}$	$1.43^{+0.30}_{-0.24}$	ms
$\log(\kappa_{\gamma})$	Ejecta gamma-ray opacity	[−4,4]	$-1.23^{+0.10}_{-0.14}$	$0.93^{1.84}_{-1.44}$	$\rm cm^2\ g^{-1}$
$M_{\rm ej}$	Ejecta mass	[0.1,100]	$3.59^{+1.06}_{-0.75}$	$21.59^{+8.22}_{-4.67}$	$M_{\odot}$
$T_{\rm min}$	Photospheric plateau temperature	[3,10]	$9.78^{+0.14}_{-0.23}$	$5.47^{+0.54}_{-0.28}$	10^3 K
$v_{\rm ej}$	Ejecta velocity	[1,20]	$7.87^{+0.50}_{-0.54}$	$6.94^{+0.28}_{-0.28}$	10^3 $\rm km\ s^{-1}$

model also includes a temperature floor for the photosphere (Nicholl et al. 2017c), which is motivated by late-time observations of SLSNe (e.g. Inserra et al. 2013; Nicholl et al. 2017a) – this plateau temperature $T_{\rm min}$ can also be checked against spectral models.

4.2 Spectrum modelling

We utilized the code named SYN++ (Thomas, Nugent & Meza 2011) to model the available spectra of SN 2021bnw and SN 2021fpl. This code uses some local parameters that fit the lines of the individual ions and global parameters referring to the entire model spectrum. The global parameters are as follows:

(i) a_0: a constant multiplier to the overall model spectrum;
(ii) $v_{\rm phot}$: the velocity at the photosphere (the uncertainty of this parameter is ∼1000 $\rm km\ s^{-1}$, for detailed explanation, see section 3.3.2 in Silverman et al. 2015); and
(iii) $T_{\rm phot}$: the temperature at the photosphere (the uncertainty of $T_{\rm phot}$ is ∼2000 K, discussed in Könyves-Tóth 2022).

The local parameters are as follows:

(i) τ: the optical depth for the reference line of each ion;
(ii) $v_{\rm min}$: the inner velocity of the line-forming region;
(iii) $v_{\rm max}$: the outer velocity of the line-forming region;
(iv) *aux*: the scale height of the optical depth above the photosphere given in $\rm km\ s^{-1}$ (this parameter accounts for the width of the spectral features that is in relation with the width of the line-forming region in the atmosphere – the larger the *aux* parameter, the broader the feature; and
(v) $T_{\rm exc}$: excitation temperature of each element/ion, assuming local thermodynamic equilibrium.

The best-fitting models obtained for the spectra of SN 2021bnw are shown in Fig. 8, while the same in case of SN 2021fpl are plotted in Fig. 9. In these figures the observed spectra are shown with black line, while green colour codes the best-fitting models built in SYN++. The single-ion contributions to the overall model spectra are denoted with turquoise lines shifted vertically for clarification. The local parameter values of the best-fitting models can be found in Tables E1 and E2 in the online supplementary material..

4.2.1 SN 2021bnw

In case of SN 2021bnw two spectra were modelled, both from the photospheric phase taken at −14- and +77-d rest-frame phase relative to the moment of the maximum light. The date of maximum was estimated from the MOSFiT fitting as MJD 59265. As shown in the left-hand panel of Fig. 8, the pre-maximum spectrum of SN 2021bnw shows some W-shaped O II features between 4000 and 5000 Å, making this object a 'type W' SLSN-I using the classification scheme of Könyves-Tóth & Vinkó (2021). According to the best-fitting SYN++ model, the velocity of the photosphere is 20 000 $\rm km\ s^{-1}$, while the photospheric temperature is 14 000 K. These are not extraordinary, but high values compared to other SLSNe. The best-fitting model of the second spectrum taken at +77-d phase (see the right-hand panel of Fig. 8) contains the features of Na I, Mg II, Si II, high-velocity Si II (Si II v), and Fe II. By this phase, the O II and C II lines have disappeared and the photospheric velocity swiftly decreased to 4000 $\rm km\ s^{-1}$ and the temperature of the photosphere dropped to 6500 K, making SN 2021bnw a spectroscopically fast evolving event.

The estimated ejecta velocity is around 8000 $\rm km\ s^{-1}$. If this is the photospheric velocity at peak, then the photospheric velocity evolution in this system was very fast at pre-peak, decreasing by a factor of ∼2.5 in 2 week, followed by a fairly slow evolution post-peak, decreasing by a factor of ∼2 in ∼2.5 month. The estimated plateau temperature is almost ∼10 000 K, which is much higher than the photospheric temperature inferred from the +77-d spectrum. This apparent discrepancy may come from model uncertainties within MOSFiT.

4.2.2 SN 2021fpl

We carried out the spectrum modelling of the −18-, −3-, +27-, and +49-d phase spectrum of SN 2021fpl, as can be seen in Fig. 9. We estimated the date of the maximum as MJD 59 350 using the MOSFiT fitting similarly to SN 2021bnw. As the top-left panel of Fig. 9 shows, the earliest phase spectrum of SN 2021fpl is differing from the −14-d phase spectrum of SN 2010bnw, as the former does not show the W-shaped O II features between 4000 and 5000 Å, and rather can be fitted using Si II and Fe II lines. This fact makes SN 2021fpl a 'type 15bn' SLSN-I by Könyves-Tóth & Vinkó (2021). The photospheric velocity ($v_{\rm phot}$ = 11 000 $\rm km\ s^{-1}$) and temperature ($T_{\rm phot}$ = 6800) K are also much lower compared to the similar phase spectrum of SN 2021bnw, strengthening that SN 2021fpl resembles to SN 2015bn by its pre-maximum spectrum evolution.

The −3-d phase spectrum of SN 2021fpl is modelled using Si II, Fe II, and Fe III lines (see the top-right panel of Fig. 9). By this time, the $v_{\rm phot}$ diminished to 6000 $\rm km\ s^{-1}$, while the best-fitting $T_{\rm phot}$ is 5700 K, a result which is broadly consistent with the MOSFiT modelling. The best-fitting model of the +27-d phase spectrum (see the bottom panel of Fig. 9) shows similar lines and has the same photospheric velocity as the −3-d phase and the photospheric

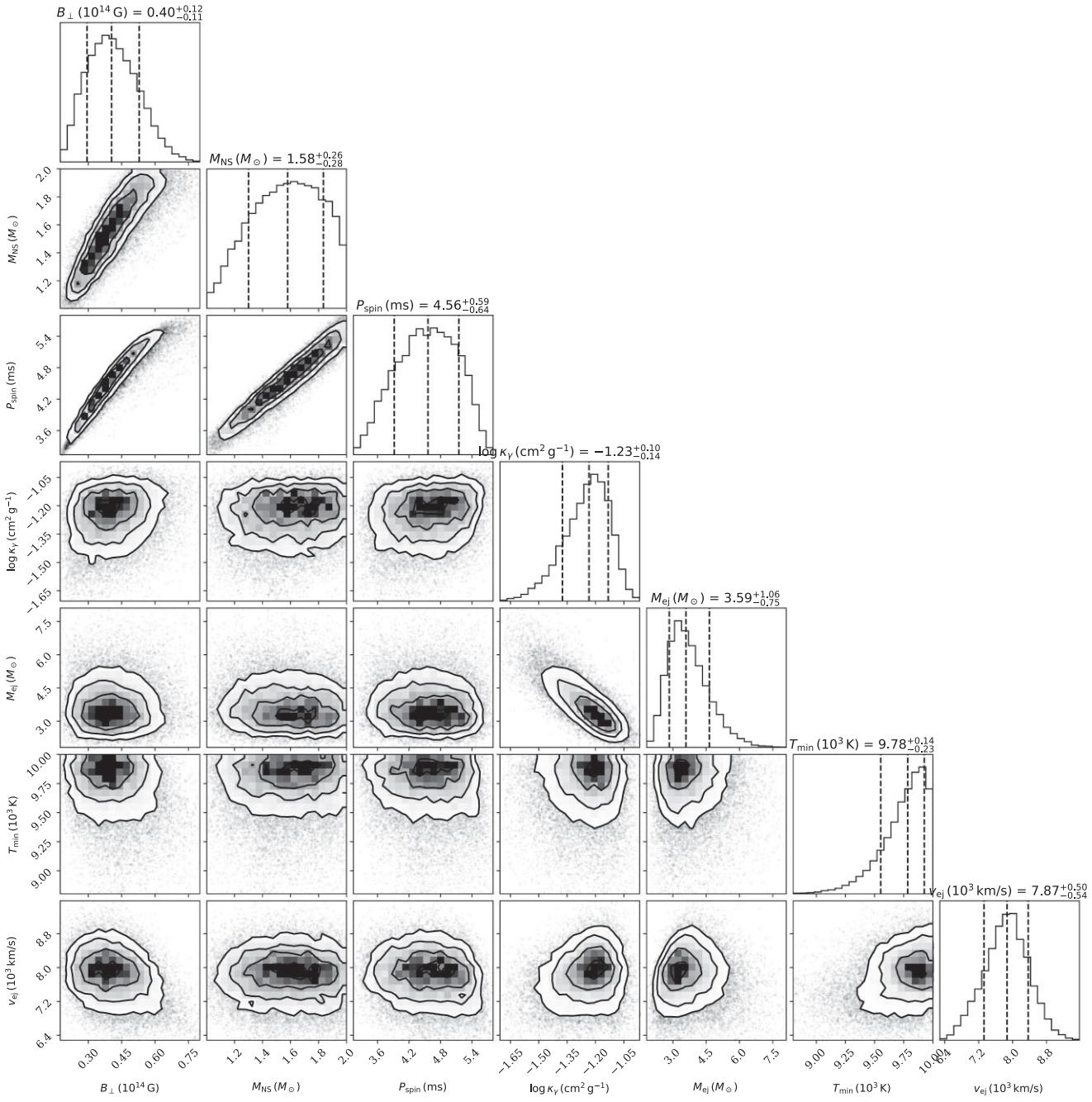

Figure 6. 1D and 2D posterior distributions of the magnetar model parameters obtained from SN 2021bnw light-curve analysis with `MOSFiT`. Median and 1σ values are marked and labelled – these are used as the best-fitting values (discussed in text).

temperature is similar as well (5200 K). This suggests that SN 2021fpl shows a spectroscopically slow evolution, like SN 2015bn. In Fig. 9, the +49-d phase observed spectrum (red line) of SN 2021fpl is plotted together with the +27-d phase spectrum (black line). It is seen that they are quite similar to each other, thus they share the best-fitting `SYN++` model.

4.3 Polarimetry analysis

The levels of polarization obtained on polarized and unpolarized calibration stars, on SN 2021bnw, on SN 2021fpl, and on several objects of interest in their field of view, are displayed in Table 3. The steps followed to get estimates of the intrinsic polarization degree of SN 2021bnw and of SN 2021fpl (see last column in Table 3) are given in the following sections. A visual summary of all these results can be seen on the $Q - U$ plots displayed in Fig. F1 for each polarimetry epoch (see online supplementary material). The polarization was corrected for bias following the equation given in Wang, Wheeler & Höflich (1997):

$$P = (P_{\rm obs} - \sigma_P^2/P_{\rm obs}) \times h(P_{\rm obs} - \sigma_P), \tag{3}$$

where h is the Heaviside function, $P_{\rm obs}$ is the observed polarization, and σ_P is the 1σ error.

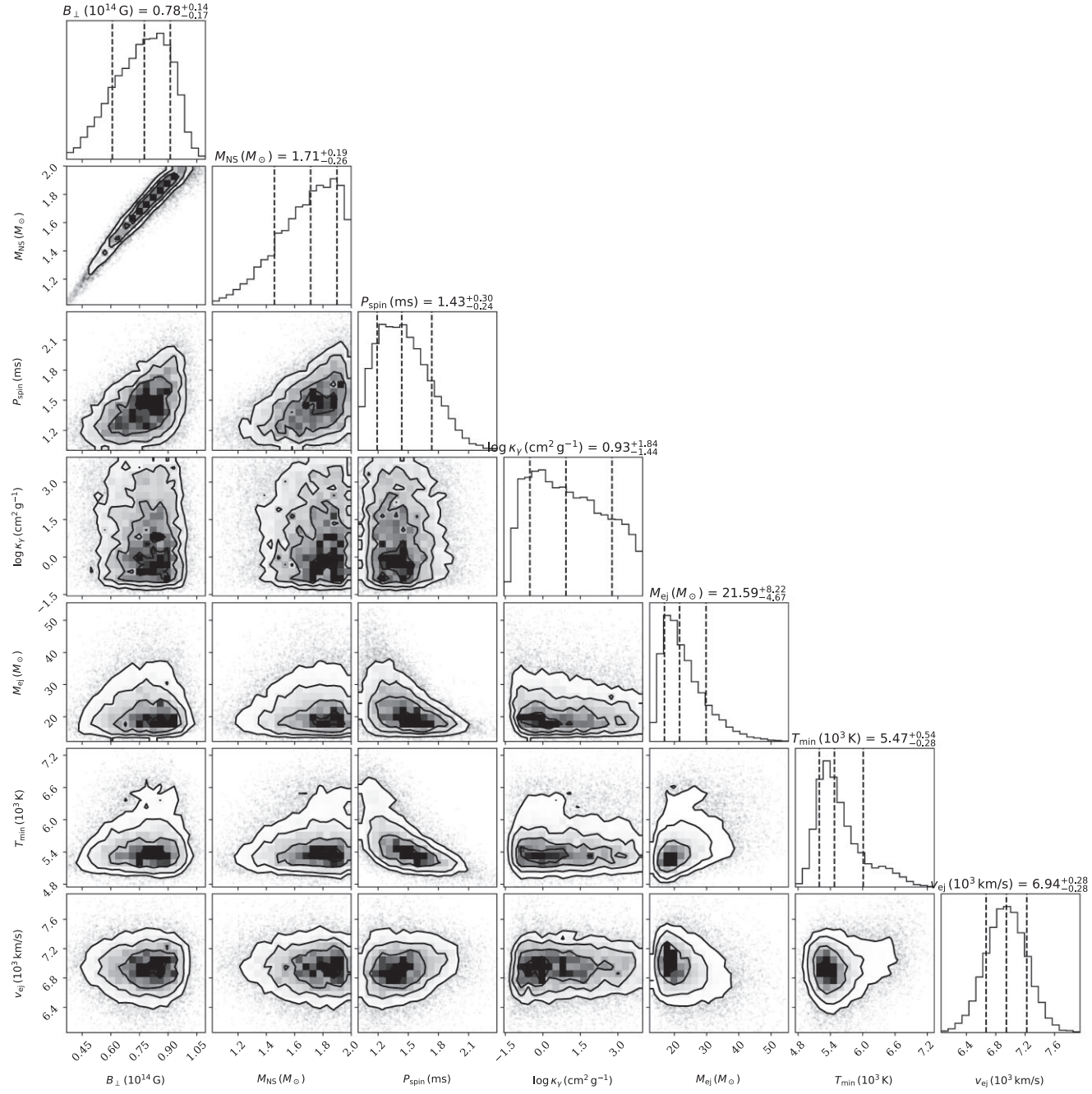

Figure 7. 1D and 2D posterior distributions of the magnetar model parameters obtained from SN 2021fpl light-curve analysis with MOSFiT. Median and 1σ values are marked and labelled – these are used as the best-fitting values (discussed in text).

4.3.1 SN 2021bnw

The degree of polarization obtained after bias correction along the line-of-sight of SN 2021bnw about 3-month after maximum light (+89 d), is $p = 0.05 \pm 0.10$ per cent. This measurement, displayed in column 8 in Table 3, was obtained after instrumental polarization (IP), and ZPA corrections only, without applying any correction to remove the polarization component foreground to the SN. Getting estimates of the Galactic polarization contribution is difficult for that source since there is no star available in the field of view covered by ALFOSC (see Fig. 3, top panel). An alternative is to look to starlight polarization of Galactic stars compiled in the catalogue provided by Heiles (2000). A few stars have been observed at distances about 6° from the position of SN 2021bnw. Relevant data retrieved from the catalogue are given in Table 4. All measurements show very low levels of polarization, with $p \leq 0.2$ per cent. The most relevant measurement is $p = 0.166 \pm 0.025$ per cent from HD 91 316 (see bold line) which heliocentric distance of 791.5 pc is the highest. If this measurement is representative of the level of polarization along the line-of-sight of SN 2021bnw, this means that one could expect that the overall level of polarization of SN 2021bnw and its host is consistent with a null-polarization degree.

Since a contribution to the degree of polarization foreground to SN 2021bnw could also come from its host galaxy, we observed

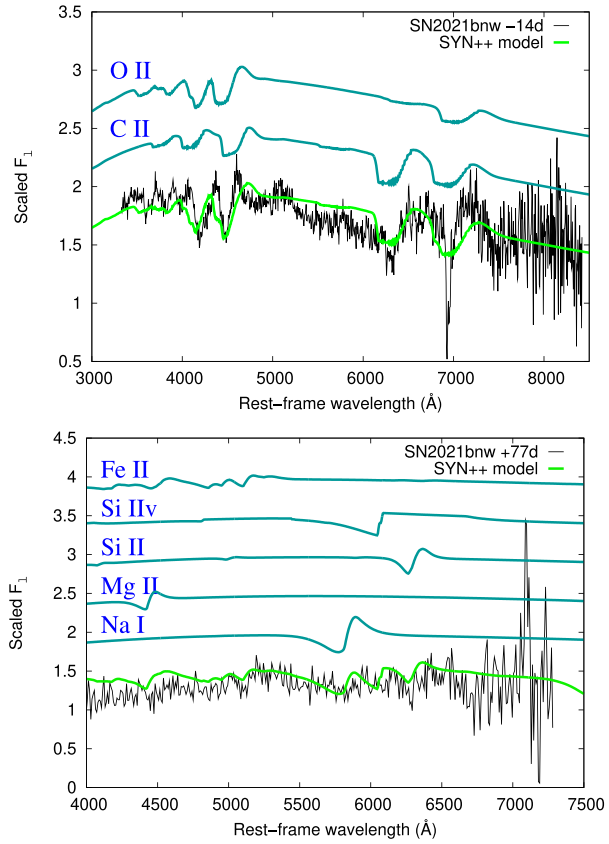

Figure 8. Top panel: Spectrum at −14 d relative to peak brightness of SN 2021bnw (black line) plotted together its best-fitting model built using SYN++ (green line). Single-ion contributions to the overall model spectrum (turquoise lines) are also plotted. Bottom panel: Spectrum at +77 d relative to peak brightness of SN 2021bnw together with its best-fitting model. The colour coding is the same as in the left-hand panel.

SN 2021bnw and its host a second time about 1-yr after maximum light (+347 d), when the SN was more than 4 magnitudes fainter than its host (see Fig. 1, top plot). After bias correction, the IP and ZPA-corrected measured degree of polarization, given in column 8 in Table 3, is $p = 0.09 \pm 0.21$ per cent. This measurement is consistent with the first epoch measurement, and at the same level than the Galactic ISP estimated from the Heiles (2000) catalogue in the vicinity of the system. Since the flux from the SN was negligible at this epoch, this means that the intrinsic degree of polarization of SN 2021bnw host galaxy is negligible and can be considered consistent with 0 per cent at both epochs. This result suggests that an intrinsic null-polarization degree was measured on SN 2021bnw during the first epoch measurement (+89 d). Assuming the galaxy is fully unpolarized, we also estimate that the total flux of the galaxy would dilute the polarization level measured on SN 2021bnw during the first polarimetry epoch at the level of 30 per cent in the *V* band. This means that the intrinsic polarization level of SN 2021bnw would be 1.3 higher than its estimated value, but still consistent with a null-polarization measurement.

4.3.2 SN 2021fpl

The degree of polarization obtained on SN 2021fpl at the four epochs is displayed in bold in the last column of Table 3. The first bias-corrected four epochs estimates ($P = 1.10 \pm 0.25$ per cent, $P = 0.70 \pm 0.23$ per cent, $P = 0.63 \pm 0.13$ per cent, and $P = 0.87 \pm 0.17$ per cent) have been obtained following one of the methods used to derive the intrinsic level of polarization on SN 2020znr in Poidevin et al. (2022) (in the following we call it METHOD 1). At each epoch the *Q* and *U* Stokes parameters measured on field stars, STAR 1, STAR 2, and STAR 3, were IP and ZPA-corrected using the unpolarized and polarized stars measurements. These measurements obtained on the three field stars were then weighted averaged to get a final estimate of the ISP from the Milky Way.

A look to columns 8 and 9 in Table 3 shows that, for each of the field star, the estimates obtained at the four epochs are almost all consistent with each other. The coordinates of these stars are

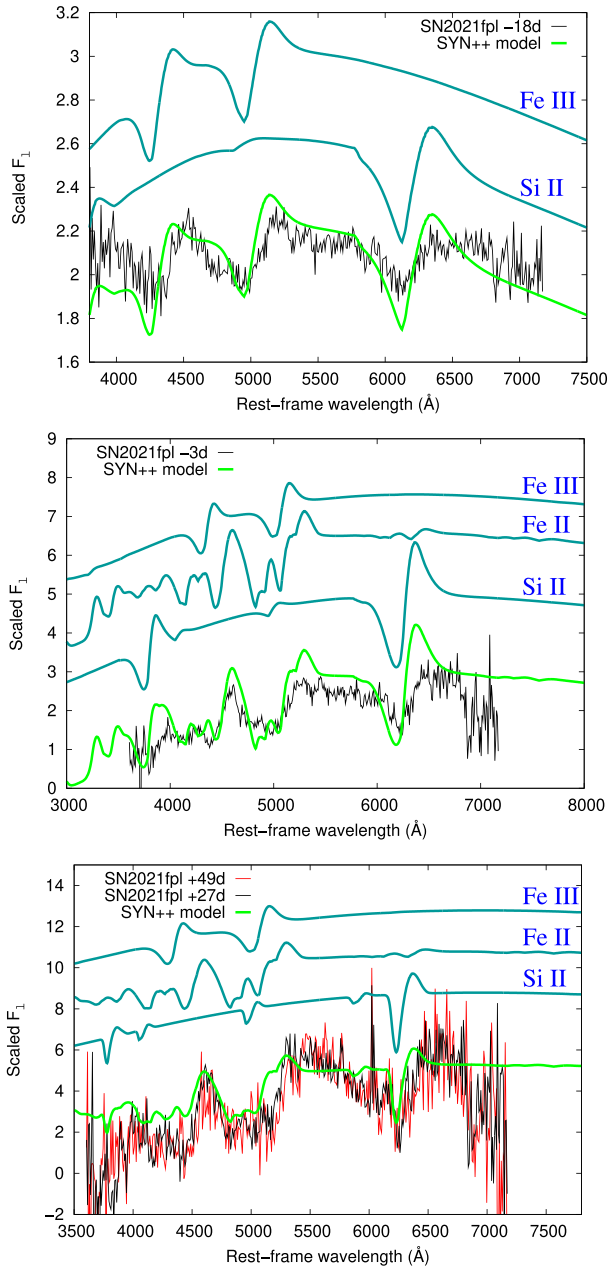

Figure 9. Top panel: Modelling the −18-d phase SN 2021fpl with SYN++. Middle panel: Modelling of the −3-d phase spectrum. Bottom panel: Modelling of the +27-d (black) and the +49-d (red) phase spectrum. The colour coding is the same as in Fig. 8.

Table 3. *V*-band polarimetry results on SN 2021bnw and its host, and on SN 2021fpl. a: Stokes parameters, $\overline{Q}$ and $\overline{U}$, directly obtained from the ALFOSC data frames extraordinary and ordinary images without applying any further corrections. b: Instrumental polarization estimates. c: Instrumental polarization-corrected. Assuming HD127769, HD251204, BD+64106, and BD+323739 have a polarization angle of 147°, the zero polarization angle (ZPA) estimates are 83.9° and 87.7°, respectively. d: IP and ZPA-corrected. e: IP and ZPA-corrected + Milky Way ISP-corrected with Stokes parameters obtained on STAR 2 (f), which is at the largest heliocentric distance, then with weighted average Stokes parameters obtained on stars STAR 1, STAR 2, and STAR 3 (g) (see text for details). (bc): Bias-corrected.

Date	Source	$\overline{Q}^a$	$\overline{U}^a$	P (per cent)^b	P (per cent)^c	θ (°)^c	P (per cent)^d	θ (°)^d	P (per cent)^e
2021-05-17	GD 319	0.03	− 0.10	**0.10 ± 0.09**	...	...	...	...	...
...	HD127769	0.45	− 1.41	...	**1.38 ± 0.11**	**143.85 ± 2.37**	...	...	...
...	SN 2021bnw	0.04	0.03	...	....	...	0.05 ± 0.10 ^{bc}	132.98 ± 20.77	...
2022-01-29	HD94851	− 0.04	− 0.08	**0.09 ± 0.08**	...	...	...	...	...
...	HD251204	− 3.10	3.73	...	**4.88 ± 0.18**	**64.38 ± 1.04**	...	...	...
...	BD+64106	5.46	1.74	...	**5.80 ± 0.11**	**9.16 ± 0.53**	...	...	...
...	SN 2021bnw host	0.00	0.00	...	....	...	0.09 ± 0.21^{bc}	− 12.25 ± 23.15	...
2021-05-16	BD+323739	0.08	0.09	**0.12 ± 0.09**	...	...	...	...	...
...	Hiltner960	1.99	− 5.51	...	**5.92 ± 0.09**	**144.40 ± 0.44**	...	...	...
...	STAR 1	− 0.84	− 0.06	...	....	...	0.94 ± 0.15	4.96 ± 4.57	...
...	STAR 2	− 0.90	0.25	...	....	...	1.00 ± 0.22	175.91 ± 6.36	...
...	STAR 3	− 0.78	− 0.01	...	....	...	0.87 ± 0.40	3.86 ± 13.26	...
...	ISP	0.00	0.00	...	....	...	**0.94 ± 0.12**	**1.63 ± 3.63**	...
...	SN 2021fpl^f	− 0.16	− 0.30	...	....	...	0.46 ± 0.23	29.60 ± 14.44	**1.10 ± 0.25**^{bc}
2021-06-13	BD+323739	0.06	0.03	**0.07 ± 0.06**	...	...	...	...	...
...	Hiltner960	1.92	− 5.30	...	**5.65 ± 0.06**	**144.58 ± 0.31**	...	...	...
...	STAR 1	− 1.02	− 0.28	...	....	...	1.12 ± 0.12	8.39 ± 3.17	...
...	STAR 2	− 0.90	− 0.14	...	....	...	0.98 ± 0.15	5.25 ± 4.35	...
...	STAR 3	− 0.55	− 0.16	...	....	...	0.64 ± 0.15	8.96 ± 6.84	...
...	ISP	0.00	0.00	...	....	...	**0.93 ± 0.08**	**7.46 ± 2.50**	...
...	SN 2021fpl^f	0.19	− 0.06	...	....	...	0.16 ± 0.22	71.80 ± 39.64	**0.70 ± 0.23**^{bc}
2021-06-28	BD+323739	0.06	− 0.04	**0.07 ± 0.03**	...	...	...	...	...
...	Hiltner960	2.06	− 5.41	...	**5.73 ± 0.06**	**145.23 ± 0.31**	...	...	...
...	STAR 1	− 0.78	− 0.03	...	....	...	0.83 ± 0.08	179.08 ± 2.64	...
...	STAR 2	− 0.58	0.05	...	....	...	0.64 ± 0.10	175.39 ± 4.31	...
...	STAR 3	− 0.52	0.11	...	....	...	0.60 ± 0.09	172.16 ± 4.51	...
...	ISP	0.00	0.00	...	....	...	**0.70 ± 0.05**	**176.21 ± 2.08**	...
...	SN 2021fpl^f	0.06	0.10	...	....	...	0.15 ± 0.13	132.89 ± 23.98	**0.63 ± 0.13**^{bc}
2021-07-08	BD+323739	0.04	0.00	**0.04 ± 0.06**	...	...	...	...	...
...	Hiltner960	1.97	− 5.45	...	**5.79 ± 0.08**	**144.74 ± 0.41**	...	...	...
...	STAR 1	− 0.89	− 0.04	...	....	...	0.93 ± 0.09	1.31 ± 2.89	...
...	STAR 2	− 0.69	− 0.18	...	....	...	0.75 ± 0.12	7.18 ± 4.71	...
...	STAR 3	− 0.71	0.13	...	....	...	0.76 ± 0.14	175.20 ± 5.12	...
...	ISP	0.00	0.00	...	....	...	**0.82 ± 0.07**	**1.38 ± 2.30**	...
...	SN 2021fpl^f	− 0.08	− 0.05	...	....	...	0.14 ± 0.17	11.70 ± 35.70	**0.87 ± 0.17**^{bc}
4 epochs	STAR 1	...	...	...	....	...	0.95 ± 0.11	3.80 ± 3.46	...
...	STAR 2	...	...	...	....	...	0.83 ± 0.15	1.05 ± 5.35	...
...	STAR 3	...	...	...	....	...	0.70 ± 0.23	0.26 ± 9.45	...
...	ISP	...	...	...	....	...	**0.85 ± 0.30**	**2.27 ± 10.09**	...
2021-05-16	SN 2021fpl^f	− 0.16	− 0.30	...	....	...	0.46 ± 0.23	29.60 ± 14.44	**0.49 ± 0.38**^{bc}
2021-06-13	SN 2021fpl^f	0.19	− 0.06	...	....	...	0.16 ± 0.22	71.80 ± 39.64	**0.84 ± 0.37**^{bc}
2021-06-28	SN 2021fpl^f	0.06	0.10	...	....	...	0.15 ± 0.13	132.89 ± 23.98	**0.77 ± 0.33**^{bc}
2021-07-08	SN 2021fpl^f	− 0.08	− 0.05	...	....	...	0.14 ± 0.17	11.70 ± 35.70	**0.57 ± 0.34**^{bc}
4 epochs	ISP (STAR 1)	...	...	...	....	...	**0.95 ± 0.11**	**3.80 ± 3.46**	...
2021-05-16	SN 2021fpl^f	− 0.16	− 0.30	...	....	...	0.46 ± 0.23	29.60 ± 14.44	**0.67 ± 0.26**^{bc}
2021-06-13	SN 2021fpl^f	0.19	− 0.06	...	....	...	0.16 ± 0.22	71.80 ± 39.64	**1.01 ± 0.25**^{bc}
2021-06-28	SN 2021fpl^f	0.06	0.10	...	....	...	0.15 ± 0.13	132.89 ± 23.98	**0.96 ± 0.17**^{bc}
2021-07-08	SN 2021fpl^f	− 0.08	− 0.05	...	....	...	0.14 ± 0.17	11.70 ± 35.70	**0.77 ± 0.20**^{bc}

Table 4. Starlight polarization from the Heiles (2000) agglomeration file catalogue in the vicinity of SN 2021bnw.

Star name	RA (J2000) (°)	Dec (J2000) (°)	GLON (°)	GLAT (°)	P (per cent)	σ_P (per cent)	θ (°)	σ_θ (°)	V (mag)	Heliocentric distance (pc)	Distance to SN 2021bnw (°)
97179.0	167.844 135	8.2670	246.8084	59.7332	0.090	0.069	53.8	21.0	9.0	436.5	6.04
91636.0	158.759 130	8.6504	236.2949	52.8599	0.080	0.120	73.0	36.9	5.6	65.0	5.99
91316.0	**158.202 810**	**9.3065**	**234.8871**	**52.7675**	**0.166**	**0.025**	**98.1**	**4.3**	**3.8**	**791.5**	**6.09**
97907.0	168.966 240	13.3075	239.9347	63.7440	0.050	0.120	50.0	50.2	5.3	87.1	5.55
97633.0	168.560 175	15.4297	235.3722	64.5853	0.010	0.120	93.0	80.5	3.3	25.0	5.80

Table 5. *Gaia* EDR3 distances to the field stars, STAR 1, STAR 2, and STAR 3, displayed in Fig. 3. Parameter, *rgeo*, is the geometric distance, while parameter, *rpgeo*, is the photogeometric distance (see Bailer-Jones et al. 2021, for details).

Star name	RA (J2000) (°)	Dec (J2000) (°)	*rgeo* (pc)	*rpgeo* (pc)
STAR 1	303.5720	−18.1781	6643.951 66	5319.877 44
STAR 2	303.5723	−18.1644	816.467 285	776.057 312
STAR 3	303.5768	−18.1864	3749.818 85	3465.271 48

displayed in Table 5. Using TOPCAT (Taylor 2005), we cross-matched the stars coordinates with the *Gaia* Early Data Release 3 (EDR3) catalogue in order to obtain estimates of the distances to each star. The median of the geometric distance posterior, *rgeo*, and the median of the photogeometric posterior, *rpgeo*, extracted from the catalogue are displayed in columns 4 and 5, respectively, in Table 5. The distance estimate to STAR 2 is of order 800 pc, while the one to STAR 3 is of about 3600 pc, and the one to STAR 1 is of order 5300 pc or higher. This seems to corroborate with the high level of polarization of order $P = 0.95 \pm 0.11$ per cent observed on STAR 1 when the four epochs measurements are weighted averaged, while similar averaged measurements obtained on STAR 2 and STAR 3, are of $P = 0.83 \pm 0.15$ per cent, and of $P = 0.70 \pm 0.23$ per cent, respectively. These values are displayed in columns 8 and 9 in Table 3, under field Date = 4 epochs. Since these three estimates are almost consistent with each other within their uncertainties, they were weighted averaged to get a first estimate of the global four epochs ISP contribution, P (ISP) $= 0.85 \pm 0.31$ per cent), and $\theta_{\rm ISP} = 2.27 \pm 10.09°$ (METHOD 2). The relatively large uncertainty on P ($\sigma_P = 0.31$ per cent) coming from this combination propagates on the intrinsic estimates of P obtained on SN 2021fpl at each epoch ($P = 0.49 \pm 0.38$ per cent, $P = 0.84 \pm 0.37$ per cent, $P = 0.77 \pm 0.33$ per cent, and $P = 0.57 \pm 0.34$ per cent), and leads to less accurate measurements than with METHOD 1.

Finally, since STAR 1 is the field star at the higher distance from the sun, we consider the four epochs weighted measurements obtained on that star, as another good proxy of the averaged ISP obtained at the four epochs (METHOD 3). The bias-corrected intrinsic levels of polarization of SN 2021fpl obtained with that method are given in the last columns of the four last rows in Table 3. Similarly to the results obtained with METHOD 1, these estimates show $>3\sigma$ measurements, leading to the possibility that the photosphere of SN 2021fpl, observed close to and after maximum light, was not symmetrical. A result that was also observed on SN 2015bn, and on SN 2017egm.

5 DISCUSSION

From the previous analysis, SN 2021bnw can be classified as a fast evolver, of spectral type W, showing no evidence of intrinsic polarization over time (−14 and +77 d in the observer frame). On the other hand, SN 2021fpl is a slow evolver, of spectral type 15bn, showing hints of intrinsic polarization after maximum light (≈ +23, +38, and +48 d in the observer frame). A summary of this information and similar information compiled on other type I SLSN observed with polarimetry is given in Table 6. The sample is obviously quite low for one to derive any strong conclusion but it is interesting to note that while polarimetry is not available before maximum light on SN 2021fpl, it is showing an intrinsic level of polarization after maximum light, as does, SN 2015bn which is also classified as a slow evolver. On the other hand, since no polarimetry was obtained earlier before maximum light, a contribution from SN 2021fpl's host galaxy cannot be discarded at this stage.

Table 6. Possible categorization of some SLSNe that have been probed with linear polarimetry.

SLSN	W/15bn[a] type	Fast/slow evolving event	P^b (per cent)
LSQ14mo	W[a]	Slow[a]	Null[c]
2015bn	15bn[a]	Slow[a, d]	Increase with time[e]
2017egm	W[f]	Fast[f]	Increase with time[g]
2018bsz	W[h]	Slow[a, i]	Change with time[h]
2020znr	W[j]	Slow[j]	Null[j]
2020ank[b]	W	Fast[b]	Null[k]
2021bnw	W[b]	Fast[b]	Null[b]
2021fpl	15bn[b]	Slow[b]	Non-zero[b]

Note. a: Könyves-Tóth & Vinkó (2021). b: This work. c: Leloudas et al. (2017b). d: Nicholl et al. (2017c). e: Inserra et al. (2016); Leloudas et al. (2017a). f: Nicholl et al. (2017b). g: Saito et al. (2020). h: Pursiainen et al. (2022). i: Anderson et al. (2018). j: Poidevin et al. (2022). k: Lee (2020).

To better understand SLSN-I polarization properties, in the following sections we first make a summary of the variation of the intrinsic (or at least ISP-corrected) linear polarization of SLSNe as a function of their empirical diffusion time-scale estimates. We then have a look at the several spectral features observed with linear polarimetry on this sample of objects. Indeed a similar filter will capture different absorption features as a function of the redshifts and phases of the transients. Such a study may help to better understand the polarization sample currently available. Then, we explore the `MOSFiT` space parameters to search for any correlation between SLSN-I polarization properties and the parameters inferred from the modelling of the light curves.

5.1 SLSNe light-curves polarimetry sampling

ISP-corrected or intrinsic polarization measurements have been obtained on SN 2015bn (Inserra et al. 2016; Leloudas et al. 2017a), SN 2017egm (Saito et al. 2020), SN 2018bsz (Pursiainen et al. 2022), SN 2021fpl (this work), SN LSQ14mo (see Leloudas et al. 2015, 2017b, with the second reference giving revised ISP-corrected polarimetry of the data presented in the first reference), SN 2020ank (Lee 2020), SN 2020znr (Poidevin et al. 2022), and SN 2021bnw (this work). The polarimetry of SN 2017egm is similar to linear polarimetry obtained from spectropolarimetry after some integration in the wavelength range of ≈4600–9400 Å, rest frame (see Saito et al. 2020). Linear polarimetry was also conducted by Maund et al. (2019) on that source but the measurements were lacking sensitivity therefore they are not included in this analysis. Similarly, the results obtained on SN 2018bsz are from spectropolarimetry after some integration in the wavelength range of ≈3200–9100 Å, rest frame. Spectropolarimetry is also available on SN 2015bn (see Inserra et al. 2016). The data obtained at two epochs integrated over the ALFOSC *V*-band filter give results consistent with those obtained with linear polarimetry by Leloudas et al. (2017a), and are included in this analysis. All these spectropolarimetry data are considered and discussed in more details in Section 5.2.

Fig. 10 (top panel) shows the distribution of the polarimetry obtained on SN 2015bn, SN 2017egm, SN 2018bsz, SN 2021fpl, SN LSQ14mo, SN 2020ank, SN 2020znr, and SN 2021bnw as a function of $\tau_{\rm diff,\,emp} + 1$ (in log scale), where $\tau_{\rm diff,\,emp}$ is the empirical diffusion time-scale. The empirical diffusion time-scales were obtained by

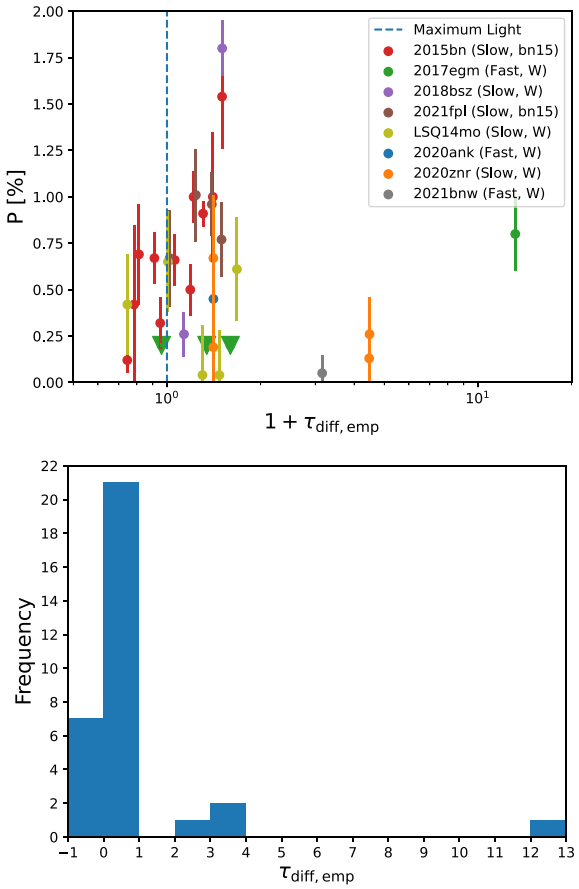

Figure 10. Top panel: Distribution of the degree of polarization as a function of the diffusion time-scale from the sample of SLSN-I for which intrinsic polarization measurements are available. Bottom panel: Histogram of the diffusion time-scales when polarimetry was obtained.

normalizing the SLSNe phases when polarimetry was measured by the rising time-scale estimates retrieved from light-curve analysis (see Table 7). Maximum light is shown by the vertical dashed line in the plot. The data spread in the empirical diffusion time-scale range −0.3–12.2. This is illustrated in the histogram displayed in Fig. 10 (bottom panel). Seven intrinsic polarization measurements are available before maximum light ($\tau_{\rm diff,\,emp} < 0$). A few of them obtained on SN 2015bn are more than 3σ detections but all of them are showing $P < 0.75$ per cent. Departures from this limit are seen after maximum light and at empirical diffusion time-scales between 0 and 1 on the transients SN 2015bn (slow evolver, bn15 type), SN 2018bsz (slow evolver, W type), and SN 2021fpl (slow evolver, 15bn type), while the remaining sources (all W type) are all showing low level of polarization ($P < 0.75$ per cent). Above $\tau_{\rm diff,\,emp} > 1$, in the empirical diffusion time-scale range $2 < \tau_{\rm diff,\,emp} < 4$, the measurements are very scarce with null-polarization detections on SN 2021bnw (fast evolver, W type) and on SN 2020znr (slow evolver, W type). Then another high polarization detection is available on SN 2017egm (fast evolver, W type) at a high empirical diffusion time-scale, $\tau_{\rm diff,\,emp} \approx 12.2$.

With a total of 32 measurements, empirical diffusion time-scales are mainly sampled by polarimetry in the range of $-1 < \tau_{\rm diff,\,emp} < 1$ (28 measurements). In that domain, independently of the spectral type, only some of the slow evolvers are showing an increase of polarization and one has to probe empirical diffusion time-scales $\tau_{\rm diff,\,emp} > 3$ to detect an increase of polarization on a fast evolver (SN 2017egm). Obviously, higher polarimetry cadence samples on a larger sample of SLSN-I and on the wide range of empirical diffusion time-scales discussed here ($-1 < \tau_{\rm diff,\,emp} < 13$) may lead to different conclusions. If such a sample was available, its interpretation could also be subject to the limit of the spectral ranges probed by linear polarimetry, when this technique is applied. For a given pass-band the spectral domain probed in the rest-frame of the SLSN will vary with the redshift and may lead to higher or lower probability to detect polarization variations. We discuss these aspects in the following section.

5.2 Spectral windows observed with polarimetry

In this section, we discuss and compare some of the spectral features integrated over the various filters used for linear polarimetry. The wavelength ranges covered by each filter and a summary of the polarimetry are given in Table 8. The polarization values of SN 2020ank (Lee 2020) and SN 2020znr (Poidevin et al. 2022) were bias-corrected using equation (3). The polarization values of SN 2015bn (Inserra et al. 2016; Leloudas et al. 2017a), SN 2017egm (Saito et al. 2020), SN LSQ14mo (Leloudas et al. 2015), and SN 2018bsz (Pursiainen et al. 2022) were already bias-corrected and are given as so. The spectra of SN 2015bn, SN 2017egm, SN PTF12dam, and SN LSQ14mo used in this section were retrieved from the WISEReP[15] (see Yaron & Gal-Yam 2012) repository. When spectra on SN 2020ank, SN 2020znr are not available at phases close to the epochs when polarimetry was obtained, the spectra of SN 2017egm and SN PFT12dam are used as spectral templates for comparisons and identification of some spectral features, respectively. If not already provided by our SYN++ analysis, this information was gathered in the literature. From one study to the other, some spectral features are sometimes described with different atomic elements. The list of the most typical features is indicated in the last column of Table 8. A summary of this information is also provided on the several plots shown in Figs 11 and 12.

5.2.1 15bn type, slow evolver

We first focus on the 15bn type. The polarimetry sample only contains slow evolvers with this spectral type. SN 2021fpl ($z = 0.115$) and SN 2015bn ($z = 0.1136$) have very similar redshift meaning that polarimetry obtained through the ALFOSC *V* band are integrating the signals over very similar wavelength ranges, making spectroscopy and polarimetry comparisons more straightforward.

Fig. 11 (top panel) shows the spectral features integrated in the linear polarimetry ALFOSC *V*-band filter during the observations close to and after maximum light of SN 2021fpl. Spectroscopy obtained before maximum light (−18 d) is also shown. The main absorption spectral features captured by the polarimetry filter around and after maximum light are produced by Fe II and Fe III, with contributions from Si II, as from the SYN++ analysis discussed in Section 4.2. The Fe III absorption may be less strong at phase −18 d than at higher phases and Fe II and Si II are not required to fit that spectrum, inferring a spectral transition phase occurred between −18 and −3 d. For comparison, SN 2015bn shows a significant spectral evolution between +7 and +20 d, with very slow spectral evolution before +7 and after +20 d (see e.g. Nicholl et al. 2016). This is illustrated with the sequence of spectra displayed in Fig. 11 (bottom panel). Before

[15]WISEReP, https://www.wiserep.org/.

Table 7. Magnetar model parameters from `MOSFiT` for some SLSNe that have been probed with linear polarimetry. The first three have shown an increase or change in polarization over time or a non-negligible level of polarization, while the rest have shown only null detections. a: If not mentioned otherwise the rise time is the estimated explosion date to *g*- or *V*-band peak, and has an uncertainty of around 10 per cent. b: Rise time estimates from Könyves-Tóth & Vinkó (2021). c: Parameters will likely be estimated in Roy et al. (in preparation). d: Fit with `MINIM` (Chatzopoulos et al. 2013).

SN name	$P_{\rm spin}$ (ms)	$B_\perp$ (10^{14} G)	$M_{\rm ej}$ ($M_\odot$)	$v_{\rm ej}$ (10^3 km s^{-1})	$M_{\rm NS}$ ($M_\odot$)	Rise time[a] (d)	Source
SN 2015bn	$2.16^{+0.29}_{-0.17}$	$0.31^{+0.07}_{-0.05}$	$11.73^{+0.83}_{-1.34}$	$5.46^{+0.16}_{-0.14}$	$1.78^{+0.28}_{-0.23}$	90.88[b]	Nicholl et al. (2017c)
SN 2017egm	$4.38^{+0.44}_{-0.67}$	$0.79^{+0.20}_{-0.22}$	$3.72^{+1.65}_{-0.90}$	$6.35^{+0.22}_{-0.22}$	$1.67^{+0.22}_{-0.33}$	16	Nicholl et al. (2017b)
SN 2018bsz[c]						76.17[b]	Anderson et al. (2018)
SN 2021fpl	$1.43^{+0.30}_{-0.24}$	$0.78^{+0.14}_{-0.17}$	$21.59^{+8.22}_{-4.67}$	$6.94^{+0.28}_{-0.28}$	$1.71^{+0.19}_{-0.26}$	96	This work
SN LSQ14mo	$4.97^{+0.65}_{-0.71}$	$1.01^{+0.27}_{-0.30}$	$2.10^{+0.42}_{-0.36}$	$10.74^{+0.52}_{-0.41}$	$1.85^{+0.22}_{-0.27}$	34.22[b]	Nicholl et al. (2017c)
SN 2020ank[d]	2.23 ± 0.51	2.09 ± 0.07	3.58 ± 0.04	12.27 ± 0.91	N/A	36	Kumar et al. (2021)
SN 2020znr	$2.80^{+0.26}_{-0.39}$	$0.52^{+0.10}_{-0.13}$	$21.37^{+1.53}_{-1.43}$	$5.56^{+0.13}_{-0.13}$	$1.68^{+0.21}_{-0.31}$	90	Poidevin et al. (2022)
SN 2021bnw	$4.56^{+0.59}_{-0.64}$	$0.40^{+0.12}_{-0.11}$	$3.59^{+1.06}_{-0.75}$	$7.87^{+0.50}_{-0.54}$	$1.58^{+0.26}_{-0.28}$	41	This work

Table 8. Polarimetry summary table. a: As from Inserra et al. (2016) after integration of the very large telescope spectropolarimetry data in the ALFOSC *V*-band filter. b: Könyves-Tóth & Vinkó (2021). c: Nicholl et al. (2013). d: Chen et al. (2017). e: This work.

SN	Redshift	MJD (max) (d)	MJD (pol) (d)	Pol. phase (d)	$\tau_{\rm diff,\,emp}$	P (per cent)	σ_P (per cent)	$\lambda_{\rm min}$ (Å)	$\lambda_{\rm max}$ (Å)	Spectral features
SN 2021fpl	0.115	59265.0	59267.0	1.8	0.02	0.67	0.26	4292.38	5782.53	Fe III, Fe II, Si II v[e]
...	...	...	59288.0	20.6	0.24	1.01	0.25	...	...	
...	...	...	59303.0	34.1	0.39	0.96	0.17	...	...	
...	...	...	59313.0	43.0	0.50	0.77	0.2	...	...	
SN 2015bn	0.1136	57102.0	57080.1	− 19.6	− 0.22	0.42	0.43	4297.77	5789.80	Fe III, Fe II[b]
...	...	...	57083.0	− 17.0	− 0.19	0.69	0.27	...	...	...
...	...	...	57093.0	− 8.1	− 0.09	0.67	0.14	...	...	...
...	...	...	57097.1	− 4.4	− 0.05	0.32	0.14	...	...	...
...	...	...	57108.0	5.4	0.06	0.66	0.14	...	...	...
...	...	...	57121.1	17.1	0.19	0.5	0.14	...	...	...
...	...	...	57124.1	19.8	0.22	1.0	0.14	...	...	...
...	...	...	57142.9	36.8	0.40	1.0	0.35	...	...	...
...	...	...	57153.0	45.8	0.50	1.54	0.28	...	...	Fe II, Si II, Si IIv[b]
...	...	...	57076.2	− 23.7[a]	− 0.25	0.12	0.07	...	...	Fe III, Fe II[b]
...	...	...	57133.0	27.5[a]	0.31	0.91	0.07	...	...	...
SN 2017egm	0.030721	57925.8	57925.2	− 0.6	− 0.04	0.2	...	4559.91	8828.77	OII[b]
...	...	...	57931.2	5.2	0.34	0.2	...	...	...	...
...	...	...	57935.2	9.1	0.60	0.2	...	...	...	...
...	...	...	58116.5	185.0	12.18	0.8	0.2	...	...	Fe II, Na I, [Ca II][c]
SN 2020ank	0.22	58894.3	58909.2	12.2	0.41	0.45	0.3	3922.95	5284.85	OII[b]
SN 2021bnw	0.098	59265.0	59354.0	81.1	2.16	0.05	0.1	4358.83	5872.06	Fe II, Na I v[e]
SN LSQ14mo	0.253	56698.9	56690.2	− 6.9	− 0.25	0.42	0.27	3817.06	5371.12	OII, (Si IIIv)[d]
...	...	...	56699.1	0.2	0.01	0.65	0.27	...	...	...
...	...	...	56709.2	8.2	0.30	0.04	0.27	...	...	Fe II, Mg II[d]
...	...	...	56715.1	12.9	0.47	0.04	0.24	...	...	...
...	...	...	56722.1	18.5	0.68	0.61	0.28	...	...	...
SN 2020znr	0.1	59233.0	59267.0	30.9	0.41	0.67	0.34	4350.91	5861.38	Fe II[c]
...	...	...	59267.0	30.9	0.41	0.19	0.32	5046.99	7747.96	Na I, Si II, [Ca II][c]
...	...	...	59521.0	261.8	3.47	0.13	0.14	...	...	...
...	...	...	59522.0	262.7	3.48	0.26	0.2	...	...	...
SN 2018bsz	0.0267	58267.5	58278.0	10.2	0.13	0.26	0.12	3300.00	9325.00	See Pursiainen et al. (2022)
...	...	...	58307.0	38.5	0.51	1.8	0.15	...	...	...

a rest-frame phase of +7 d, SN 2015bn is very lowly polarized ($P \approx$ 0.5 per cent) while the level of polarization is higher after +20 d (see results summarized in Table 8, results displayed in the bottom plot in Fig. 11 and Leloudas et al. 2017a). The level of polarization of SN 2021fpl before maximum light is not known therefore we do not know if SN 2021fpl underwent a polarization transition phase as did SN 2015bn (Inserra et al. 2016; Leloudas et al. 2017a), during its spectral transition phase. On the other hand, despite their mild quality, the spectra, at phases −3, +27, and +49 d, obtained on SN 2021fpl show similar spectral structures to those seen in the spectra obtained on SN 2015bn after ≈+20 d (see Fig. 11, bottom panel). This gives support to the possibility that SN 2021fpl underwent a polarization transition phase earlier than SN 2015bn. As mentioned previously, SN 2015bn was observed with spectropolarimetry by Inserra et al. (2016) at two epochs, one pre-peak at −23.7 d, and another 27.5 d after maximum in the rest frame. The analysis of the variation of the polarization shows the presence of a dominant axis in the $Q - U$ plane with no departure from it which is interpreted

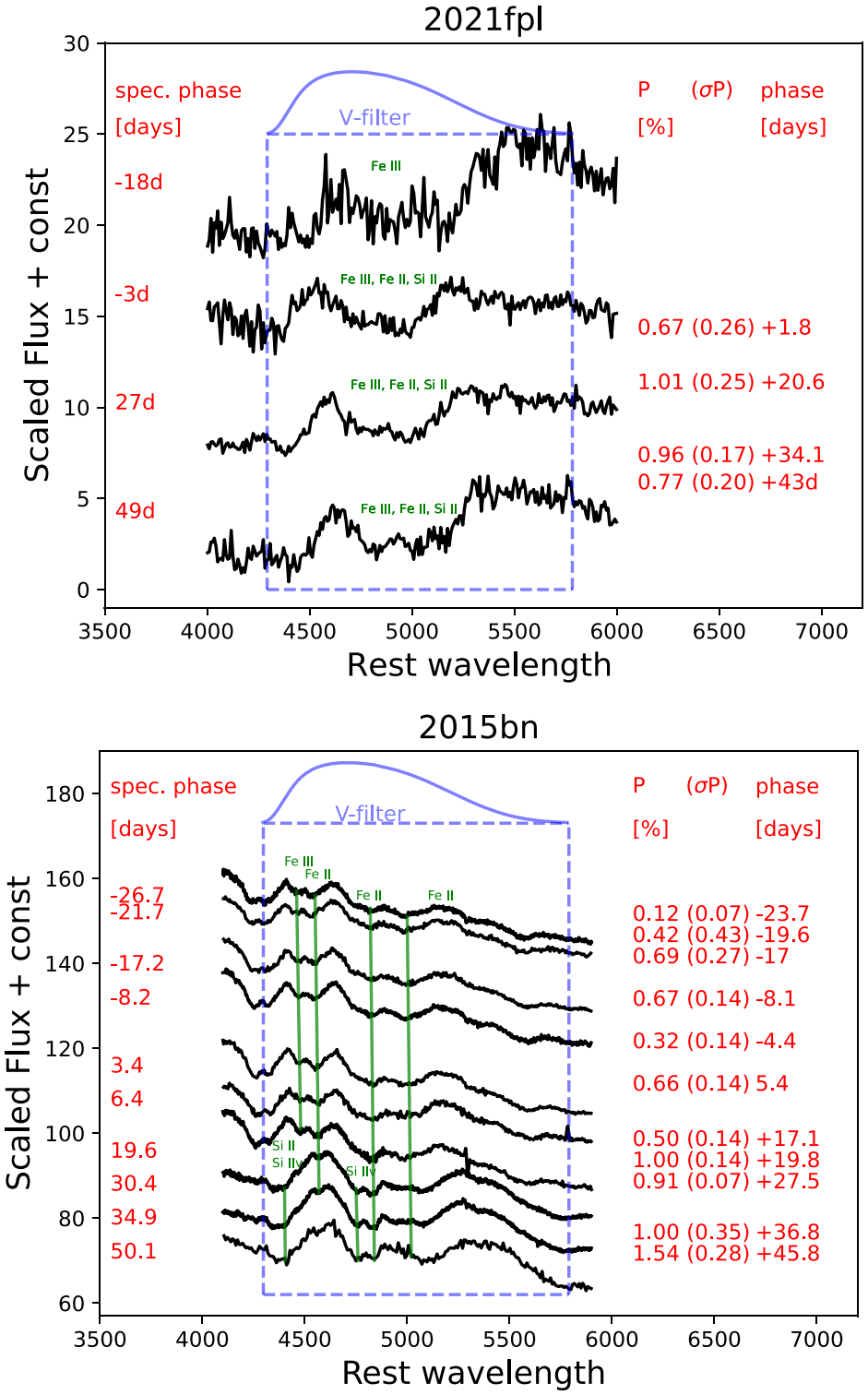

Figure 11. Spectral features observed in the rest-framed *NOT* ALFOSC Bessel *V* filter. Top panel: SN 2021fpl. Bottom panel: SN 2015bn. The phases when spectroscopy and polarimetry were obtained are indicated in red. The levels of polarization are also given. The filter band-passes are shown in blue and with the blue boxes. The main absorption spectral features integrated over the filters are shown in green.

as the axis of symmetry of the inner photosphere. This result was confirmed by Leloudas et al. (2017a) with the linear polarimetry data discussed before. The data obtained on SN 2021fpl also show the presence of a dominant axis over the period of about 40-d rest frame during which polarimetry was acquired from about maximum light. The polarization angles obtained from the first to the fourth epochs given in the last four lines in Table 3 are $\theta = 79.4^\circ \pm 9.9$, $\theta = 90.8^\circ \pm 6.6$, $\theta = 98.0^\circ \pm 4.9$, and $\theta = 92.5^\circ \pm 7.1$, respectively. This is another interesting point suggesting that SN 2021fpl and SN 2015bn could have similar polarization properties and are part of the same

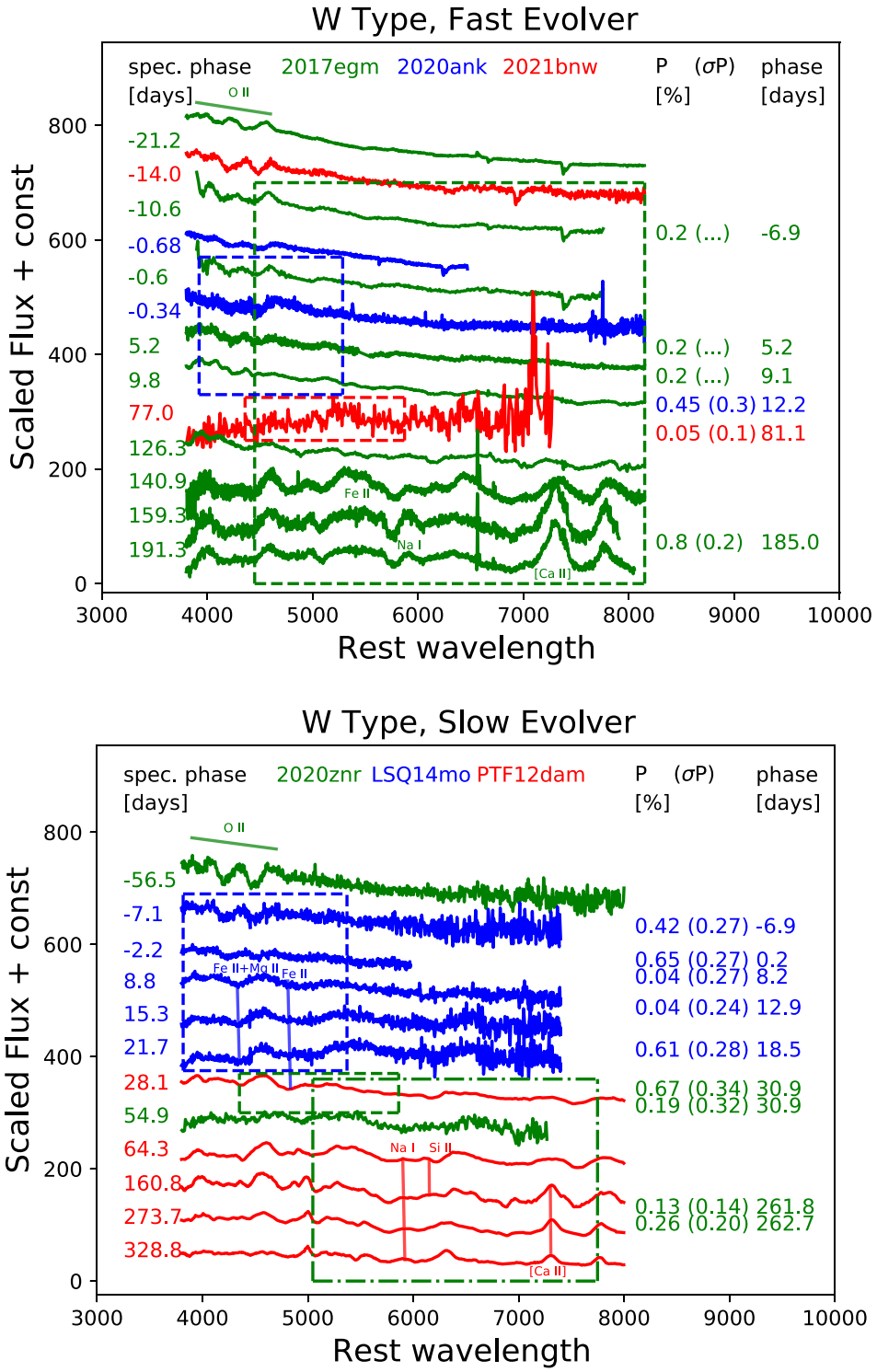

Figure 12. Top plot: Spectra of the W type, fast evolvers SN 2017egm (green), SN 2020ank (blue), and SN 2021bnw (red). The rest-framed *NOT* ALFOSC Bessel *V* filters are shown with the red box for SN 2021bnw, and with the blue box for SN 2020ank. The phases when spectroscopy and polarimetry were obtained are indicated in the plot, as well as the levels of polarization. Bottom plot: Same as top plot but for the slow evolvers SN 2020znr (green), LSQ14mo (blue), and PTF12dam (red). The rest-framed *V*-filters wavelength ranges are shown with the blue and with the small green dashed line boxes. The wide green dashed line box shows the wavelength range covered by the *NOT* ALFOSC Bessel *R* filter that was used to observe SN 2020znr.

class of objects. The intrinsic levels of polarization measured after SN 2015bn and SN 2021fpl underwent a spectroscopic transition are very similar to each other which also supports this hypothesis. If this is the correct this means that, similarly to SN 2015bn, the ellipticity of the photosphere of SN 2021fpl could have receded from an initially external layer with a prolate geometry of axis ratio $a/c \approx 0.9$ where $b = c$, keeping its geometry over time while the inner shell would have increased its asphericity from ≈0.9 to ≈0.6,

as from the quantitative model proposed by Inserra et al. (2016) to interpret the increase of intrinsic linear polarization of SN 2015bn.

5.2.2 W Type, fast evolver

SN 2017egm was observed with spectropolarimetry at four epochs by Saito et al. (2020). A sequence of some of the spectra publicly available on WISEReP is shown in green in Fig. 12. The wavelength range over which Saito et al. (2020) made simple average of the polarization was between 4450 and 8150 Å. This is illustrated by the dashed line green box in the figure. Also plotted in the figure are the publicly available spectra of SN 2020ank shown in blue, and the spectra of SN 2021bnw shown in red and discussed in this work. All together, these spectra show the spectral evolution one could roughly expect for each of these SLSN. The dashed blue box shows the wavelength range of the *V*-band filter used for polarimetry on SN 2020ank by Lee (2020). One could expect the spectral feature integrated over the filter about 12 d after maximum light was mainly the well-known W-shape absorption feature produced by O II and C II, as from the analysis of the −14-d rest-frame spectrum of SN 2021bnw discussed in Section 4.2. This feature is partly captured by the bandwidth used to derive the polarization level of SN 2017egm shown with the green dashed box. All put together these results show a consistent picture suggesting that the photosphere of the W type, fast evolvers is still almost spherical until a few weeks after maximum light during which the W feature is still visible, i.e. the photospheres have prolate geometry of axis-ratio of order 0.9–0.95 (see Hoflich 1991).

The filter used for polarimetry on SN 2021bnw about 80 d after maximum light is shown with the red dashed box. The low level of polarization obtained in this filter suggests that the spectral features now produced by Fe II and Na I are associated to a photosphere still almost spherical. At later phase around +185 d, SN 2017egm underwent an increase of polarization which interpretation is complex (see discussion in Saito et al. 2020). The increase in polarization could come from a loss of symmetry on the inner photosphere, but additional late epochs polarimetry would have been helpful to show if the change of polarization stands along a dominant axis as for SN 2015bn, or if it was produced by some interactions with a clumpy CSM. The Fe II and Na I already observed at earlier phase in the +77-d spectrum of SN 2021bnw are visible in the spectra of SN 2017egm close to that epoch and, for that reason, may be rejected as the cause of the change in polarization.

5.2.3 W Type, slow evolver

SN 2018bsz has been observed with spectropolarimetry and the results are discussed by Pursiainen et al. (2022). The spectra of SN 2018bsz exhibit several features commonly seen in SLSNe but its spectral evolution looks uncommon among the W, slow evolver type discussed here, with multicomponent H_α profile appearing about +30 d after maximum light. The polarization results obtained by Pursiainen et al. (2022) are compiled in Table 8 and show a measurement consistent with null-polarization after maximum light (+10.2 d) while a relatively high level of polarization $P = 1.80 \pm 0.15$ per cent is found after maximum light (+38.4 d). In that case the ISP is unknown and there was a fairly significant change in polarization angle between the two epochs, for these reasons the increase of polarization is most likely explained by highly aspherical, possibly disc-like, CSM with several emitting regions. For all the aforementioned reasons, we did not add SN 2018bsz to the plot in Fig. 12 (bottom panel). On the other hand a sequence of spectra including spectra of SN 2020znr (shown in green), of LSQ14mo (shown in blue), and of SN PTF12dam (shown in red) is show in that figure. The spectra of SN PTF12dam are assumed to be representative of the W, slow evolver type at epochs when polarimetry was obtained on SN 2020znr, without a spectroscopy counterpart.

In Fig. 12, the blue dashed box shows the bandwidth of the *V* filter used to get polarimetry on SN LSQ14mo by Leloudas et al. (2015). The final results given by Leloudas et al. (2017b) are also given in the plot. As for fast evolvers, the W-shape spectral feature associated to O II seems not to be polarized (−7.1 d). After that epoch the spectra show LSQ14mo underwent a spectral evolution with spectral features likely and mainly produced by Fe II and Mg II around 4300 Å (see Chen et al. 2017). The lack of high-SNR polarization measurements obtained after maximum light on that source suggest none of these spectral features could give insight on a loss of symmetry on the inner ejecta. The same is found at later epoch (+30.9 d) with the polarimetry of SN 2020znr in the *V*-filter spectral window shown with the green dashed box. The same conclusion is corroborated by the results obtained towards the *R*-filter window shown with the green dash–dotted box in the plot. At later epoch, the *V*-band filter was not used and the spectral window does not include the spectral features in the wavelength range of 4000–5000 Å.

5.2.4 Synthesis of the results

The results discussed in the previous section suggest than none of the several spectral groups of SLSN-I show a substantial level of polarization before maximum light. If it happens, a change of polarization property seems rather to occur after a spectral transition of the photosphere. Regarding the 15bn group, the previous analysis suggests that SN 2021fpl underwent a spectral evolution similar to SN 2015bn, and possibly a polarization evolution as well, even though, no polarimetry is available at early phase on SN 2021fpl. On the contrary, it looks like the W-type SLSNe, SN 2020ank, SN 2021bnw, SN 2020znr, and SN LSQ14mo, whether they are slow or fast evolvers, did not undergo a polarization transition, except maybe in the case of SN 2017egm. In this spectral class, the increase of polarization observed on SN 2017egm (+185 d) lack additional polarimetry data epochs to know if the polarization would have evolved along a dominant axis. From the spectral analysis, though, it looks like the early and late spectra of SN 2017egm show H_α emission features likely coming from its host galaxy, and detected when the flux of the SLSN was not dominating the one of the galaxy. The shape of the H_α emission features is not suggesting interactions with a clumpy CSM and the increase of polarization could therefore be a probe of a loss of symmetry of the inner photosphere. From the identification or compilation of the spectral features observed by polarimetry and summarized in Table 8 it is difficult to associate any specific element to an increase of polarization. As mentioned by Saito et al. (2020) some late-phase line profiles are sensitive to the element distribution while the continuum polarization are sensitive to the distribution of the free electron which produce polarization, therefore specific studies of these two effects would be needed to disentangle them.

5.3 Light-curve modelling parameter space

Based on the preceding analysis, and assuming that all SLSNe in the sample share a common progenitor that could be described by a magnetar model, we produce a comparison of the `MOSFiT`

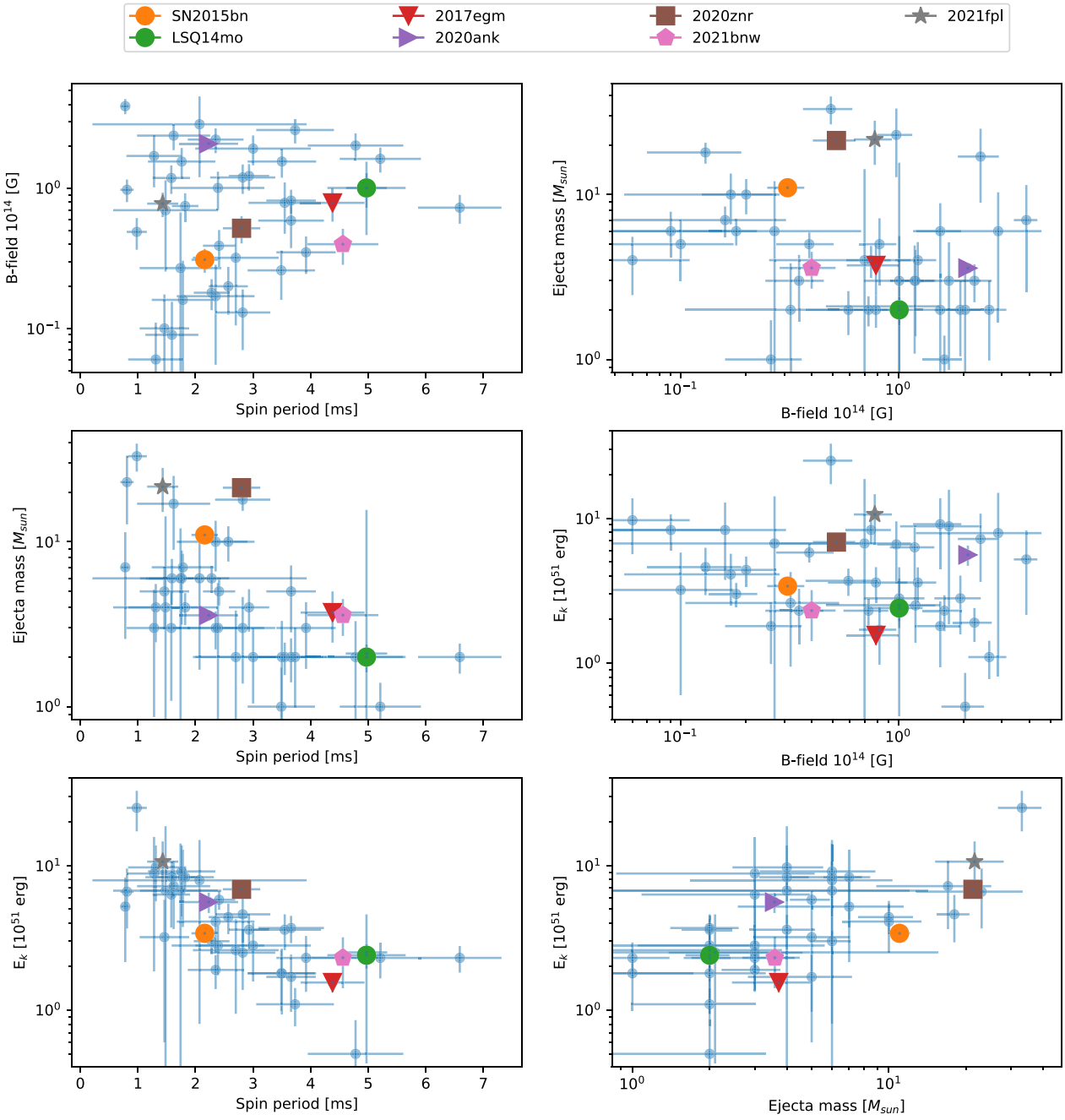

Figure 13. Distribution of the MOSFiT best-fitting magnetar model parameters as from Nicholl et al. (2017a). Overplotted with different coloured symbols are the parameters obtained on SN 2015bn, SN 2017egm, SN LSQ14mo, SN 2020ank, SN 2020znr, SN 2021bnw, and SN 2021fpl given in Table 7, for which polarimetry data are available.

best-fitting parameters obtained with that model. Fig. 13 shows the distribution of the MOSFiT best-fitting parameters as from Nicholl et al. (2017a) and retrieved from their work. Overplotted are the parameters obtained on SN 2015bn, SN 2017egm, SN LSQ14mo, SN 2020ank, SN 2020znr, SN 2021bnw, and SN 2021fpl given in Table 7. In each plot, it is interesting to note that the MOSFiT best-fitting parameters of SN 2021fpl (grey star symbol) and SN 2015bn (orange disc symbol) are quite close to each other in the parameter space. The only other source, close to these two sources in each of the six plots, and on which polarimetry is available is the W-type SN 2020znr. The data at hand do not show that SN 2020znr underwent a polarization transition, may be because observations were obtained in the *R*-filter only (see plot in Fig. 12, bottom panel). On the other hand, the parameters obtained for SN 2017egm share a distinct locus in the parameter space with SN LSQ14mo and SN 2021bnw, which might imply that later polarization measurements on them (which would have been too faint to be observed) would have been interesting test beds of W-type polarization properties. Finally, we point out that the kinetic energy estimate of SN 2021fpl is slightly higher than the one of SN 2015bn while SN 2015bn has twice the spin period of SN 2021fpl and a lower magnetic field. This means that the magnetar from SN 2021fpl released its energy a lot faster than SN 2015bn,

which might give us hints about the possibility that the polarization transition phase of SN 2021fpl could have occurred earlier than the one of SN 2015bn. If this is true, from its position in the plot of E_k versus spin period, SN 2020ank would also be polarized, which is not. However, the parameter inference for SN 2020ank was done using MINIM instead of MOSFiT, which may have systematic and model differences. All these facts, put together, may indicate that 15bn-type SLSNe have different polarization properties than W-type SLSNe but surely a larger polarimetry sample with higher cadence, ideally in both *V* and *R* filters, or with spectropolarimetry, is needed to test that hypothesis.

6 CONCLUSIONS

Understanding polarization properties of H-poor SLSNe to retrieve information from their inner photospheres that could help to understand the nature of their progenitor is not an easy problem to deal with. Its looks reasonable to assume that before maximum light, SLSN-I photospheres are almost spherical (Inserra et al. 2016; Pursiainen et al. 2023; this work) with low linear polarization mainly produced by Thomson scattering of light from free electrons, and this independently of the viewing angle of the inner system. According to the SYN++ analysis the photosphere temperatures of SN 2021bnw (W type) were higher compared to those of SN 2021fpl (15bn type) consistently with Könyves-Tóth (2022) when polarimetry was obtained on each of these sources. In such a case, the electron-scattering opacities could have dominated over the line opacities. This could be one reason why measuring an increase of polarization after maximum light on 15bn-type SLSNe-I is more likely to happen than on W-type SLSNe-I, even though the 15bn-type represents only about 33 per cent of poor hydrogen SLSNe (Könyves-Tóth 2022).

In addition to this point, it is interesting to note that none of the light curves of SN 2021bnw and SN 2021fpl show any strong bumps or undulations after maximum light, contrary to what can be seen, e.g. from the light curves of SN 2018bsz, SN 2017egm, and 2017gci (see plot in fig. 5 of Pursiainen et al. 2023). After that stage, the light curves are rather smoothly decreasing. It looks therefore reasonable to assume that none of the polarization measurements obtained on these two SLSNe were possibly 'contaminated' by polarization components that would be produced by interactions of the photospheres with the CSM, which is an important point raised by Pursiainen et al. (2023). The presence of a dominant axis in the $Q - U$ plane observed on SN 2021fpl also strengthen that hypothesis.

Finally, element mixing and clumpiness could also be additional sources of complexity on the interpretation of the polarization results (Tanaka et al. 2017). At late times, once they reach the nebular phase, the inner ejecta of SLSNe becomes visible and constraints on the nucleosynthesis and core structure from spectral analysis and modelling point out to clumped ejecta (Jerkstrand et al. 2017). SLSNe produced by stronger engines could imply more mixing and clumping in the ejecta, and possibly additional sources of asymmetry in the system, than for SLSNe produced by weaker engines (Suzuki & Maeda 2021). From this point of view, SN 2015bn, SN 2021fpl, and SN 2020znr are all located in the upper left part of the spin period versus ejecta mass diagram (see Fig. 13), and can therefore be considered as strong engines. For SN 2015bn and SN 2021fpl, the increase of polarization, or high level of polarization, detected after optical maximum light could be favoured by higher mixing and clumping than from weaker engines. On the other hand, as it is mentioned by Pursiainen et al. (2023), SN 2020znr (W type) was observed with polarimetry during the nebular phase but there was no detection of an increase of polarization on that source in that phase (Poidevin et al. 2022). In this case, it could be that the temperature of its photosphere was still high enough to prevent the detection of the effects of a high level of mixing, or that the mass of the ejecta was so high that effect of its clumpy structure was still not detectable in the *R*-filter used for linear polarimetry, or both. It is worth noting that clumping and asymmetry can strongly affect other signals as well, such as nebular spectra (Jerkstrand et al. 2017; Dessart 2019; Omand & Jerkstrand 2022) and non-thermal emission (Suzuki & Maeda 2021) in radio (Omand, Kashiyama & Murase 2018; Eftekhari et al. 2019, 2021; Law et al. 2019; Murase et al. 2021), and X-rays (Kotera, Phinney & Olinto 2013; Metzger et al. 2014; Murase et al. 2015; Vurm & Metzger 2021), which may lead to correlation between polarization and these signals.

Modelling of H-poor SLSN photosphere evolution and fuller analysis of a larger observation sample might be really helpful to explore all these scenarios.

7 SUMMARY

In this work, we present new photometric, spectroscopic, and imaging polarimetry data combined with publicly available data to study some of the physical properties of the two H-poor SLSN SN 2021bnw and SN 2021fpl. The spectroscopy data were obtained with *LT* SPRAT. The polarimetry data were obtained on the *NOT* with ALFOSC in the *V*-band filter. The photometry data were obtained on SN 2021fpl with *LT* IO:O. From the analysis of these data we find that:

(i) For each SLSN, the best-fitting parameters obtained from the magnetar model with MOSFiT do not depart from the range of parameter obtained on other SLSNe discussed in the literature.

(ii) An analysis of the spectra with SYN++ shows that SN 2021bnw is a W type, fast evolver, while SN 2021fpl is a 15bn type, slow evolver.

(iii) An analysis of the polarimetry data shows no departure from null polarization for SN 2021bnw after maximum light (+81.1-d rest frame), while $>3\sigma$ polarization measurements in the range of 0.8–1 per cent are obtained for SN 2021fpl at four epochs close to and after maximum light (+1.8, +20.6, +34.1, and +43.0 d).

These results are compared with results obtained on SN 2020ank, SN 2020znr, SN 2017egm, SN 2015bn, LSQ14mo, and SN 2018bsz, a sample of SNSLe for which constrained polarization measurements are available in the literature. From these comparisons we find that:

(i) The majority of the polarimetry was obtained at diffuse time-scale ranging between −1 and 1.

(ii) SN 2021fpl underwent a spectroscopic transition as bit earlier than SN 2015, during which it could also have undergone a polarization transition.

(iii) None of the photospheres of the W-type SLSNe, whether they are slow or fast evolvers, show a clear evidence of a departure from symmetry at empirical diffusion time-scale <2. The only exception being SN 2017egm which showed an increase of polarization at an empirical diffusion time-scale of about 12.

(iv) Measurements at higher empirical diffusion time-scale may be needed to see any departure from symmetry of the W-type group.

ACKNOWLEDGEMENTS

The authors would like to thank David Morate for his kind support on the *Nordic Optical Telescope* (*NOT*), and David Young for the

ATLAS python public code he developed to stack and bin ATLAS forced photometry public data.

FP acknowledges support from the Spanish State Research Agency (AEI) under grant number PID2019-105552RB-C43. FP acknowledges support from the Agencia Canaria de Investigación, Innovación y Sociedad de la Información (ACIISI) under the European FEDER (FONDO EUROPEO DE DESARROLLO REGIONAL) de Canarias 2014-2020 grant number PROID2021010078. I.P.-F. acknowledges support from the Spanish State Research Agency (AEI) under grant numbers ESP2017-86852-C4-2-R and PID2019-105552RB- C43. R.K.T. has been supported by the NKFIH/OTKA FK-134432 grant of the National Research, Development and Innovation Office of Hungary (NKFIH) and by the ÚNKP-22-4 New National Excellence Program of the Ministry for Culture and Innovation from the source of the National Research, Development and Innovation Fund.

This work is based on observations made with the *NOT*, owned in collaboration by the University of Turku and Aarhus University, and operated jointly by Aarhus University, the University of Turku, and the University of Oslo, representing Denmark, Finland, and Norway, the University of Iceland, and Stockholm University at the Observatorio del Roque de los Muchachos, La Palma, Spain, of the Instituto de Astrofisica de Canarias. The data presented here were obtained in part with ALFOSC, which is provided by the Instituto de Astrofisica de Andalucia (IAA) under a joint agreement with the University of Copenhagen and *NOT*. Some of the data were obtained during CAT service observation Spanish time. ALFOSC polarimetry imaging data of SN2020ank and calibration data were retrieved from the *NOT* public archive.

The *Liverpool Telescope* is operated on the island of La Palma by Liverpool John Moores University in the Spanish Observatorio del Roque de los Muchachos of the Instituto de Astrofisica de Canarias with financial support from the UK Science and Technology Facilities Council.

This work is based in part on observations obtained with the 48-inch *Samuel Oschin Telescope* at the Palomar Observatory as part of the Zwicky Transient Facility project. ZTF is supported by the NSF under grant AST-1440341 and a collaboration including Caltech, IPAC, the Weizmann Institute for Science, the Oskar Klein Center at Stockholm University, the University of Maryland, the University of Washington, Deutsches Elektronen-Synchrotron and Humboldt University, Los Alamos National Laboratories, the TANGO Consortium of Taiwan, the University of Wisconsin at Milwaukee, and the Lawrence Berkeley National Laboratory. Operations are conducted by the Caltech Optical Observatories (COO), the Infrared Processing and Analysis Center (IPAC), and the University of Washington (UW).

This work has made use of data from the Asteroid Terrestrial-impact Last Alert System (ATLAS) project. The ATLAS project is primarily funded to search for near earth asteroids through NASA grants NN12AR55G, 80NSSC18K0284, and 80NSSC18K1575; byproducts of the NEO search include images and catalogues from the survey area. This work was partially funded by Kepler/K2 grant J1944/80NSSC19K0112 and HST GO-15889, and STFC grants ST/T000198/1 and ST/S006109/1. The ATLAS science products have been made possible through the contributions of the University of Hawaii Institute for Astronomy, the Queen's University Belfast, the Space Telescope Science Institute, the South African Astronomical Observatory, and The Millennium Institute of Astrophysics (MAS), Chile.

Lasair is supported by the UKRI Science and Technology Facilities Council and is a collaboration between the University of Edinburgh (grant ST/N002512/1) and Queen's University Belfast (grant ST/N002520/1) within the LSST:UK Science Consortium.

This research has made use of 'Aladin sky atlas' developed at CDS, Strasbourg Observatory, France 2000A&AS..143...33B and 2014ASPC..485..277B.

SNID is Copyright (C) 1999–2007 Stéphane Blondin and John L. Tonry, and is available under the GNU General Public License.

This work made use of the python public code `astropy/photutils: 1.0.2` release developed by Bradley et al. (2021).

This research made use of the Transient Name Server (TNS) which is the official IAU mechanism for reporting new astronomical transients such as supernova candidates, As of 2016 January 1.

This research made use of DESI LS DR9 data. The Legacy Surveys consist of three individual and complementary projects: the Dark Energy Camera Legacy Survey (DECaLS; Proposal ID #2014B-0404; PIs: David Schlegel and Arjun Dey), the Beijing-Arizona Sky Survey (BASS; NOAO Prop. ID #2015A-0801; PIs: Zhou Xu and Xiaohui Fan), and the Mayall z-band Legacy Survey (MzLS; Prop. ID #2016A-0453; PI: Arjun Dey). DECaLS, BASS, and MzLS together include data obtained, respectively, at the *Blanco* telescope, Cerro Tololo Inter-American Observatory, NSF's NOIRLab; the *Bok* telescope, Steward Observatory, University of Arizona; and the *Mayall* telescope, Kitt Peak National Observatory, NOIRLab. The Legacy Surveys project is honoured to be permitted to conduct astronomical research on Iolkam Du'ag (Kitt Peak), a mountain with particular significance to the Tohono O'odham Nation.

NOIRLab is operated by the Association of Universities for Research in Astronomy (AURA) under a cooperative agreement with the National Science Foundation.

This project used data obtained with the Dark Energy Camera (DECam), which was constructed by the Dark Energy Survey (DES) collaboration. Funding for the DES Projects has been provided by the U.S. Department of Energy, the U.S. National Science Foundation, the Ministry of Science and Education of Spain, the Science and Technology Facilities Council of the United Kingdom, the Higher Education Funding Council for England, the National Center for Supercomputing Applications at the University of Illinois at Urbana-Champaign, the Kavli Institute of Cosmological Physics at the University of Chicago, Center for Cosmology and Astro-Particle Physics at the Ohio State University, the Mitchell Institute for Fundamental Physics and Astronomy at Texas A&M University, Financiadora de Estudos e Projetos, Fundacao Carlos Chagas Filho de Amparo, Financiadora de Estudos e Projetos, Fundacao Carlos Chagas Filho de Amparo a Pesquisa do Estado do Rio de Janeiro, Conselho Nacional de Desenvolvimento Cientifico e Tecnologico and the Ministerio da Ciencia, Tecnologia e Inovacao, the Deutsche Forschungsgemeinschaft, and the Collaborating Institutions in the DES. The Collaborating Institutions are Argonne National Laboratory, the University of California at Santa Cruz, the University of Cambridge, Centro de Investigaciones Energeticas, Medioambientales y Tecnologicas-Madrid, the University of Chicago, University College London, the DES-Brazil Consortium, the University of Edinburgh, the Eidgenossische Technische Hochschule (ETH) Zurich, Fermi National Accelerator Laboratory, the University of Illinois at Urbana-Champaign, the Institut de Ciencies de l'Espai (IEEC/CSIC), the Institut de Fisica d'Altes Energies, Lawrence Berkeley National Laboratory, the Ludwig Maximilians Universitat Munchen and the associated Excellence Cluster Universe, the University of Michigan, NSF's NOIRLab, the University of Nottingham, the Ohio State University, the University of Pennsylvania, the University of Portsmouth, SLAC National Accelerator Laboratory, Stanford University, the University of Sussex, and Texas A&M University.

The Legacy Surveys imaging of the DESI footprint is supported by the Director, Office of Science, Office of High Energy Physics of the U.S. Department of Energy under Contract No. DE-AC02-05CH1123, by the National Energy Research Scientific Computing Center, a DOE Office of Science User Facility under the same contract; and by the U.S. National Science Foundation, Division of Astronomical Sciences under Contract No. AST-0950945 to NOAO.

DATA AVAILABILITY

For science reproducibility purposes the spectra presented in this work are available via WISEReP (Yaron & Gal-Yam 2012). The photometry data displayed in Table D1 to Table D3 and Table D4 to Table D7 will be available online.

REFERENCES

Anderson J. P. et al., 2018, A&A, 620, A67
Angus C. R. et al., 2019, MNRAS, 487, 2215
Bailer-Jones C. A. L., Rybizki J., Fouesneau M., Demleitner M., Andrae R., 2021, AJ, 161, 147
Bellm E. C. et al., 2019, PASP, 131, 018002
Blanchard P. K., Berger E., Nicholl M., Villar V. A., 2020, ApJ, 897, 114
Blondin S., Tonry J. L., 2007, ApJ, 666, 1024
Bradley L. et al., 2021, astropy/photutils: 1.0.2, Zenodo, available at: https://zenodo.org/record/4453725#.ZCGDii8w30o
Brennan S. J., Fraser M., 2022, A&A, 667, A62
Brown P. J. et al., 2016, ApJ, 828, 3
Chambers K. C. et al., 2016, preprint (arXiv:1612.05560)
Chatzopoulos E., Wheeler J. C., Vinko J., Horvath Z. L., Nagy A., 2013, ApJ, 773, 76
Chen K.-J., 2021, Int. J. Mod. Phys. D, 30, 2130001
Chen T. W. et al., 2017, A&A, 602, A9
Chen Z. H. et al., 2023a, ApJ, 943, 41
Chen Z. H. et al., 2023b, ApJ, 943, 42
Cikota A. et al., 2018, MNRAS, 479, 4984
Deckers M., Prentice S., Maguire K., Dimitriadis G., Magee M., Harvey L., Terwel J., 2021a, Transient Name Serv. AstroNote, 136, 1
Deckers M., Prentice S., Maguire K., Dimitriadis G., Magee M., Harvey L., Terwel J., 2021b, Transient Name Serv. Classif. Rep., 2021-1365, 1
Dessart L., 2019, A&A, 621, A141
Dexter J., Kasen D., 2013, ApJ, 772, 30
Eftekhari T. et al., 2019, ApJ, 876, L10
Eftekhari T. et al., 2021, ApJ, 912, 21
Fremling C., 2021, Transient Name Serv. Discovery Rep., 2021-326, 1
Gal-Yam A., 2019, ARA&A, 57, 305
Guillochon J., Nicholl M., Villar V. A., Mockler B., Narayan G., Mandel K. S., Berger E., Williams P. K. G., 2018, ApJS, 236, 6
Heiles C., 2000, AJ, 119, 923
Higson E., Handley W., Hobson M., Lasenby A., 2019, Stat. Comput., 29, 891
Hoflich P., 1991, A&A, 246, 481
Howell D. A., 2017, in Alsabti A. W., Murdin P., eds, Handbook of Supernovae. Springer International Publishing, Berlin, p. 431
Inserra C. et al., 2013, ApJ, 770, 128
Inserra C., Bulla M., Sim S. A., Smartt S. J., 2016, ApJ, 831, 79
Jerkstrand A. et al., 2017, ApJ, 835, 13
Kangas T. et al., 2022, MNRAS, 516, 1193
Kasen D., Bildsten L., 2010, ApJ, 717, 245
Kasen D., Woosley S. E., Heger A., 2011, ApJ, 734, 102
Könyves-Tóth R., 2022, ApJ, 940, 69
Könyves-Tóth R., Vinkó J., 2021, ApJ, 909, 24
Könyves-Tóth R., Thomas B. P., Vinkó J., Wheeler J. C., 2020, ApJ, 900, 73
Kotera K., Phinney E. S., Olinto A. V., 2013, MNRAS, 432, 3228
Kumar A. et al., 2020, ApJ, 892, 28
Kumar A. et al., 2021, MNRAS, 502, 1678
Law C. J. et al., 2019, ApJ, 886, 24
Lee C.-H., 2019, ApJ, 875, 121
Lee C.-H., 2020, Astron. Nachr., 341, 651
Leloudas G. et al., 2015, ApJ, 815, L10
Leloudas G. et al., 2017a, ApJ, 837, L14
Leloudas G. et al., 2017b, ApJ, 843, L17
Leloudas G. et al., 2022, Nature Astron., 6, 1193
Liljegren S., Jerkstrand A., Barklem P. S., Nyman G., Brady R., Yurchenko S. N., 2022, preprint (arXiv:2203.07021)
Magee M., Terwel J., Prentice S., Harvey L., Strotjohann N. L., 2021, Transient Name Serv. Classif. Rep., 2021-338, 1
Maund J. R., Steele I., Jermak H., Wheeler J. C., Wiersema K., 2019, MNRAS, 482, 4057
Maund J. R., Leloudas G., Malesani D. B., Patat F., Sollerman J., de Ugarte Postigo A., 2020, MNRAS, 498, 3730
Maund J. R. et al., 2021, MNRAS, 503, 312
Metzger B. D., Vurm I., Hascoët R., Beloborodov A. M., 2014, MNRAS, 437, 703
Moriya T. J., Sorokina E. I., Chevalier R. A., 2018, Space Sci. Rev., 214, 59
Murase K., Kashiyama K., Kiuchi K., Bartos I., 2015, ApJ, 805, 82
Murase K. et al., 2021, MNRAS, 508, 44
Nicholl M., 2021, Astron. Geophys., 62, 5.34
Nicholl M. et al., 2013, Nature, 502, 346
Nicholl M. et al., 2016, ApJ, 826, 39
Nicholl M., Berger E., Margutti R., Blanchard P. K., Milisavljevic D., Challis P., Metzger B. D., Chornock R., 2017a, ApJ, 835, L8
Nicholl M., Berger E., Margutti R., Blanchard P. K., Guillochon J., Leja J., Chornock R., 2017b, ApJ, 845, L8
Nicholl M., Guillochon J., Berger E., 2017c, ApJ, 850, 55
Omand C. M. B., Jerkstrand A., 2022, preprint (arXiv:2211.04502)
Omand C. M. B., Kashiyama K., Murase K., 2018, MNRAS, 474, 573
Omand C. M. B., Kashiyama K., Murase K., 2019, MNRAS, 484, 5468
Onken C. A. et al., 2019, Publ. Astron. Soc. Aust., 36, e033
Piascik A. S., Steele I. A., Bates S. D., Mottram C. J., Smith R. J., Barnsley R. M., Bolton B., 2014, in Ramsay S. K., McLean I. S., Takami H., eds, Proc. SPIE Conf. Ser. Vol. 9147, Ground-based and Airborne Instrumentation for Astronomy V. SPIE, Bellingham, p. 91478H
Planck Collaboration I, 2020, A&A, 641, A1
Poidevin F., Omand C. M. B., Pérez-Fournon I., Clavero R., Shirley R., Marques-Chaves R., Jimenez Angel C., Geier S., 2022, MNRAS, 511, 5948
Pursiainen M. et al., 2022, A&A, 666, A30
Pursiainen M. et al., 2023, preprint (arXiv:2301.08111)
Quimby R. M. et al., 2018, ApJ, 855, 2
Rau A. et al., 2009, PASP, 121, 1334
Saito S. et al., 2020, ApJ, 894, 154
Silverman J. M., Vinkó J., Marion G. H., Wheeler J. C., Barna B., Szalai T., Mulligan B. W., Filippenko A. V., 2015, MNRAS, 451, 1973
Smartt S. J. et al., 2017, Nature, 551, 75
Smith K. W. et al., 2019, Res. Note. Am. Astron. Soc., 3, 26
Speagle J. S., 2020, MNRAS, 493, 3132
Steele I. A. et al., 2004, Proc. SPIE Conf. Ser. Vol. 5489, Ground-based Telescopes. SPIE, Bellingham, p. 679
Suzuki A., Maeda K., 2021, ApJ, 908, 217
Tanaka M., Maeda K., Mazzali P. A., Kawabata K. S., Nomoto K., 2017, ApJ, 837, 105
Taylor M. B., 2005, in Shopbell P., Britton M., Ebert R., eds, ASP Conf. Ser. Vol. 347, Astronomical Data Analysis Software and Systems XIV. Astron. Soc. Pac., San Francisco, p. 29
Terwel J. et al., 2021, Transient Name Serv. AstroNote, 51, 1
Thomas R. C., Nugent P. E., Meza J. C., 2011, PASP, 123, 237
Tonry J. L. et al., 2018, PASP, 130, 064505
Tonry J. et al., 2021, Transient Name Serv. Discovery Rep., 2021-771, 1
Vurm I., Metzger B. D., 2021, ApJ, 917, 77
Wang L., Wheeler J. C., Höflich P., 1997, ApJ, 476, L27
Wang S. Q., Wang L. J., Dai Z. G., Wu X. F., 2015, ApJ, 799, 107

Woosley S. E., 2010, ApJ, 719, L204
Yaron O., Gal-Yam A., 2012, PASP, 124, 668

SUPPORTING INFORMATION

Supplementary data are available at *MNRAS* online.

Appendix A. LT IO:O observation logs.
Appendix B. Spectroscopy observation logs.
Appendix C. ALFOSC polarimetry observation logs.
Appendix D. Photometry table.
Appendix E. Spectrum modelling.
Appendix F. $Q - U$ plots.

Please note: Oxford University Press is not responsible for the content or functionality of any supporting materials supplied by the authors. Any queries (other than missing material) should be directed to the corresponding author for the article.

This paper has been typeset from a TEX/LATEX file prepared by the author.